ACS APPLIED MATERIALS & INTERFACES

Research Article

www.acsami.org

Systematic Investigation of Organic Photovoltaic Cell Charge Injection/Performance Modulation by Dipolar Organosilane Interfacial Layers

Charles Kiseok Song,[†] Alicia C. White,[‡] Li Zeng,[§] Benjamin J. Leever,[⊥] Michael D. Clark,[⊥] Jonathan D. Emery,[#] Sylvia J. Lou,[†,¶] Amod Timalsina,[†] Lin X. Chen,*[,†,¶] Michael J. Bedzyk,*[,§,#] and Tobin J. Marks*[,†,#]

[†]Department of Chemistry and the Argonne-Northwestern Solar Energy Research Center, Northwestern University, 2145 Sheridan Road, Evanston, Illinois 60208, United States

[‡]Weinberg College of Arts and Science, Northwestern University, 1918 Sheridan Road, Evanston, Illinois 60208, United States

[§]Graduate Program in Applied Physics, Northwestern University, 2220 Campus Drive, Evanston, Illinois 60208, United States

[⊥]Air Force Research Laboratory, 2941 Hobson Way, Wright-Patterson AFB, Ohio 45433, United States

[#]Department of Materials Science and Engineering, Northwestern University, 2220 Campus Drive, Evanston, Illinois 60208, United States

[¶]Chemical Sciences and Engineering Division, Argonne National Laboratory, Argonne, Illinois 60439, United States

Supporting Information

ABSTRACT: With the goal of investigating and enhancing anode performance in bulk-heterojunction (BHJ) organic photovoltaic (OPV) cells, the glass/tin-doped indium oxide (ITO) anodes are modified with a series of robust silane-tethered bis(fluoroaryl)amines to form self-assembled interfacial layers (IFLs). The modified ITO anodes are characterized by contact angle measurements, X-ray reflectivity, ultraviolet photoelectron spectroscopy, X-ray photoelectron spectroscopy, grazing incidence X-ray diffraction, atomic force microscopy, and cyclic voltammetry. These techniques reveal the presence of hydrophobic amorphous monolayers of 6.68 to 9.76 Å thickness, and modified anode work functions ranging from 4.66 to 5.27 eV. Two series of glass/ITO/IFL/active layer/LiF/Al BHJ OPVs are fabricated with the active layer = poly(3-hexylthiophene):phenyl-C_{71}-butyric acid methyl ester (P3HT:PC_{71}BM) or poly[[4,8-bis[(2-ethylhexyl)-oxy]benzo[1,2-b:4,5-b']dithiophene-2,6-diyl][3-fluoro-2-[(2-ethylhexyl)-carbonyl]-thi-eno[3,4-b]thiophenediyl]]:phenyl-C_{71}-butyric acid methyl ester (PTB7:PC_{71}BM). OPV analysis under AM 1.5G conditions reveals significant performance enhancement versus unmodified glass/ITO anodes. Strong positive correlations between the electrochemically derived heterogeneous electron transport rate constants (k_s) and the device open circuit voltage (V_{oc}), short circuit current (J_{sc}), hence OPV power conversion efficiency (PCE), are observed for these modified anodes. Furthermore, the strong functional dependence of the device response on k_s increases as greater densities of charge carriers are generated in the BHJ OPV active layer, and is attributable to enhanced anode carrier extraction in the case of high-k_s IFLs.

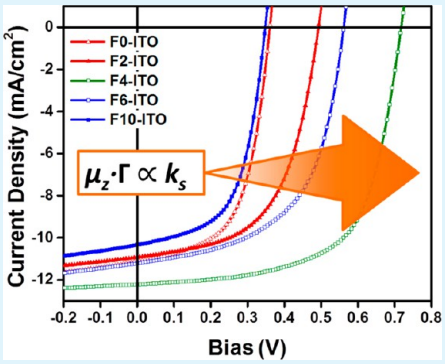

KEYWORDS: *self-assembled monolayer, organic photovoltaics, heterogeneous electron transfer rate constant, work function, open circuit voltage, power conversion efficiency*

INTRODUCTION

The insertion of interfacial layers (IFLs) between the active layer and transparent anode in bulk-heterojunction (BHJ) organic photovoltaic cells (OPVs) plays a vital role in enhancing device performance. Appropriately tailored IFLs enhance physical adhesion of the active layer to the anode, hence improving device durability,[1,2] as well as reducing electron leakage currents, hence affording higher power conversion efficiencies (PCEs) by functioning as electron blocking layers (EBLs).[3−5] The importance of nanoscopic EBLs was demonstrated previously in structurally analogous small molecular organic and polymer light-emitting diodes (OLEDs, PLEDs).[4,6,7] By confining injected charges to the emissive layer using organosilane-tethered arylamine IFLs, significant increases in quantum efficiency are observed.[4,6,7] The IFLs also mediate the surface energy mismatches between the hydrophilic ITO electrode and normally hydrophobic light-emitting active layer polymer film, thereby preventing

Received: July 29, 2013
Accepted: August 13, 2013
Published: August 13, 2013

   dx.doi.org/10.1021/am4030609 | ACS Appl. Mater. Interfaces 2013, 5, 9224−9240

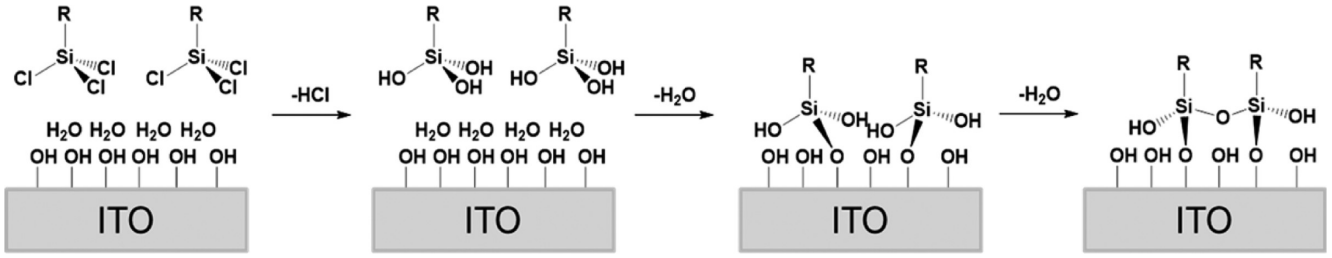

Figure 1. Schematic of organosilane chemisorption onto ITO surfaces. Chlorosilyl moieties first hydrolyze, and then condense with surface −OH groups and cross-link to form a stable film.[1].

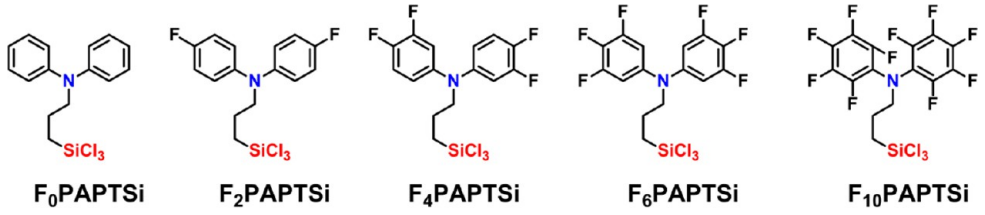

Figure 2. Molecular structures of the **F$_n$PAPTSi** series of IFL precursors examined in this study.

dewetting/delamination of the active layer, and thus enhancing PLED and OLED performance and lifetime.[8−10]

The dominant IFL material used in conventional architecture OPV fabrication is currently PEDOT:PSS, which can yield PCEs as high as 7.4%, as reported in the peer-reviewed literature.[11] However, despite the attractive properties of PEDOT:PSS as an IFL, it has several innate undesirable properties. The corrosive sulfonic acid moieties shorten device lifetime by corroding the ITO anode[12,13] and decomposing active layer materials.[14,15] The electrically inhomogeneous structure of PEDOT:PSS IFLs impede uniform contact formation[16−18] and charge transport,[19−22] and PEDOT:PSS diffusion into the active layer after device fabrication also erodes the device lifetime.[23]

New classes of OPV IFL materials have recently attracted significant research attention with the aim of addressing the limitations of PEDOT:PSS. Self-assembled monolayers (SAMs),[24−28] cross-linked conducting polymers,[2] reduced graphene oxide,[29,30] inorganic oxides,[31] and ferroelectric polymers[32] have all been implemented as anodic IFLs in OPVs, and some of them are reported to afford higher device performance than PEDOT:PSS IFLs.[31−33] These IFLs typically lack acidic or basic moieties, have superior thermal durability,[1] and in some cases enhance charge separation in the active layer.[32] Several of these IFLs have permanent dipole moments (μ) and shift electrode work functions via mechanisms that are empirically noted to enhance device performance but are not entirely understood. Although general aspects of OPV IFL dipole moment magnitude and orientation are well-documented,[24,26,27] a complete structure−function picture remains incomplete. For example, recent evidence reveals that the changes in the anode work function (Φ_s) do not linearly correlate with OPV performance because of inadequate accounting for charge selectivity in the work function term.[28,33−35]

In this contribution, we describe the systematic modulation of OPV performance metrics via insertion of a series of robust organosilane-based dipolar monolayer anode IFLs.[36] Organosilane-based SAMs are well-known to be exceedingly resistant to chemical and thermal degradation,[9,37,38] with the in-plane cross-linked Si−O−Si networks promoting dense molecular packing (Figure 1).[37,39−41] Indeed, the versatile reactivity of organosilane coupling agents with surface −OH groups forms the basis of many robust commercial coatings technologies.[42] Electrode work function modification by organosilane chemisorption is also well documented,[40,43−46] and organic electronic devices have been fabricated with silane-modified electrodes.[24,25,47,48] The excellent stability of organosilane SAMs and their capacity to modify electronic device performance makes them particularly attractive as IFLs for enhancing the performance of current-generation OPVs.

Herein we describe the synthesis, characterization, and chemisorptive properties of a series of *N*,*N*-diarylamino-*N*-propanyltrichlorosilane SAM precursors (**F$_n$PAPTSi**, Figure 2). This series was chosen because the aryl group substitution pattern can be used to systematically vary the density functional theory (DFT)-computed dipole moments, while maintaining relatively constant molecular dimensions.

Furthermore, the aryl substituents stabilize these SAM IFLs by screening the most reactive site, the N atom, while stabilizing the arylamine cation radical that is essential for hole extraction at the anode.[9,49] The N center enforces a nearly coplanar disposition of the aryl groups[50,51] and the anchoring alkyl tether chain, minimizing the SAM molecular volume, and therefore maximizing the surface packing density versus an sp^3 carbon-only counterpart. With the SAM precursors in Figure 2, the direction of the anchored SAM dipole moment on ITO will be negative, oriented toward the active layer and positive toward the electrode. This should facilitate hole injection into the ITO electrode for increased anode charge selectivity of BHJ OPVs.[24,28,33,43,46,52]

A conventional OPV architecture (Figure 3) is used in this study to fabricate a series of devices with the IFL-modified ITO anodes and two different BHJ OPV active materials.[11,31,53] The variation in the OPV response is investigated as a function of the microstructural and electronic properties of the modified ITO surfaces, with OPV performance compared to non-modified ITO anodes and PEDOT:PSS coated ITO anodes. We report that device performance is significantly enhanced by implementing IFL-modified ITO compared to bare glass/ITO anodes, and that electrode work function effects appear to be less significant than the electrode surface charge transfer rates

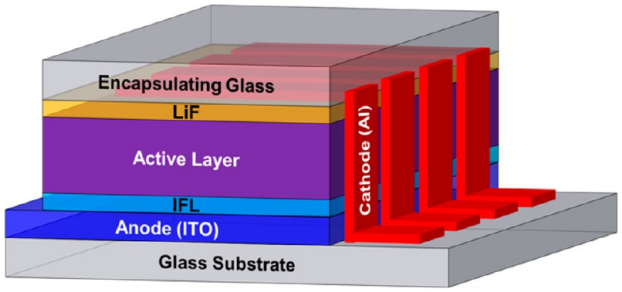

Figure 3. Schematic representation of the conventional OPV device architecture used in this study. This structure allows for four pixels that function as individual OPVs with only a single pixel is exposed to light at any time. All four pixels share a common glass substrate (gray), anode (blue), IFL on the anode (light blue), active layer (purple), hole blocking layer (LiF, orange). Each red bar denotes the cathode of a device pixel. The IFL coating on the ITO represents a select SAM-IFL or PEDOT:PSS.

in terms of modifying OPV performance parameters. In fact, a strong positive correlation is observed between all device performance metrics and k_s, the surface heterogeneous electron transport rate constant.

EXPERIMENTAL SECTION

A. Interfacial Layer Synthesis. All reactions were carried out by following a strict Schlenk protocol. All reagents were from Sigma-Aldrich and used as received unless otherwise indicated. Predried toluene and hexane from Sigma-Aldrich were dried further by passing through a Grubbs column, and anhydrous acetonitrile was used for all syntheses. ^{1}H and ^{19}F NMR spectra were measured at 500 MHz by Agilent INOVA 500 and at 376 MHz by Agilent DDR2 instruments, respectively; all ^{13}C NMR spectra were measured at 126 MHz on a Bruker AVANCE III instrument with a direct cryoprobe. High-resolution mass spectra (HRMS) were measured with an Agilent 6210A LC-TOF high-resolution mass spectrometer coupled to Agilent 1200 series HPLC stack or by a Waters GCT-Premier mass spectrometer with an Agilent 7910 series GC and EI ionization source. Elemental analyses (EAs) were determined at Midwest Microlabs, LCC., and the theoretical and experimental values are provided. All molecules were analyzed by computational methods prior to syntheses to prescreen for effective IFLs.

N-Phenyl-N-2-propen-1-ylbenzenamine. To a clean and dried Schlenk flask (200 mL) was added *N*-phenylbenzenamine (1.99 g, 11.8 mmol) from Alfa Aesar without further purification, and then the flask was connected to a Schlenk line. Acetonitrile (18 mL), potassium carbonate (3.63 g, 26.3 mmol), and tetrabutylammonium iodide (0.21g, 0.569 mmol) were added into the flask.[54] The solution was purged with N_2 for 5 min, and then stirred for 10 min at room temperature. Allylbromide (2.1 mL, 24.1 mmol) was then added and the flask was heated to 84 °C in an oil bath. The reaction mixture was stirred for 17 h, and then cooled to a room temperature. The solution was diluted with distilled water (40 mL) and the product was extracted with ethyl acetate (3 × 15 mL). The organic layer was concentrated under reduced pressure, and then purified by silica gel column chromatography with hexane as the eluent. The first band (blue colored band upon long UV radiation) was collected, reduced under vacuum, and yielded a pale yellow oil that was determined to be the product (2.06 g, 9.84 mmol, 83.4%). ^{1}H NMR ($CDCl_3$): δ 7.25 (m, 4H); 7.05 (d, 4H); 6.95 (t, 2H); 5.95 (m, 1H); 5.20 (dd, 2H); 4.38 (d, 2H); ^{13}C NMR ($CDCl_3$): δ 147.8, 134.3, 129.2, 121.2, 120.7, 116.4, 54.8. HRMS: m/z calcd for $C_{15}H_{16}N$ $[M+H]^+$: 210.1277. Found: 210.1297 (−9.47 ppm). EA calcd for $C_{15}H_{15}N$: C, 86.08; H, 7.22; N, 6.69. Found: C, 85.96; H, 7.17; N, 6.74.

N-(3-Trichlorosilylpropyl)-N-phenylbenzenamine (F_0PAPTSi). To a clean and dried Schlenk flask (25 mL) were added *N*-phenyl-*N*-2-propen-1-ylbenzenamine (0.208 g, 0.994 mmol), trichlorosilane (0.79 mL, 7.8 mmol), a small grain of chloroplatinic acid hydrate, and distilled and degassed dichloromethane in a glovebox.[6] The mixture was stirred for 5 h and the remaining reactants and solvents were removed under reduced pressure. A solvent mixture of toluene and hexane (10 mL, 1:1 v/v) was added by a syringe and a needle. The solution was filtered through a syringe filter (0.22 μm) into another Schlenk flask (25 mL), and the solvent was removed under reduced pressure. The product was a pale yellow oil (0.208 g, 0.603 mmol, 60.7%). ^{1}H NMR: ($CDCl_3$) δ 7.31 (m, 4H); 6.98 (m, 6H); 3.80 (t, 2H); 1.85 (t, 2H); 1.46 (m, 2H); ^{13}C NMR ($CDCl_3$): δ 147.78; 129.58; 121.77; 121.08; 53.67; 21.77; 20.58.

4-Fluoro-N-(4-fluorophenyl)-benzenamine. To a clean and dried Schlenk flask (200 mL) were added tris[dibenzylideneacetone]-dipalladium(0) (0.4121 g, 3.0 mol %), tri(*tert*-butyl)phosphine (0.091 g, 3.0 mol %), and sodium *tert*-butoxide (1.73 g, 18 mmol) in a glovebox.[55] The flask was connected to a Schlenk line, and then anhydrous hexane (80 mL) was added. Next, 4-fluoro-1-benzenamine (1.44 mL, 15 mmol) and 4-bromo-1-fluorobenzene (1.65 mL, 15 mmol) were added. The reaction mixture was stirred at 60 °C overnight, and then cooled to room temperature. The product was purified by silica gel chromatography eluting with hexane. The first band was collected and concentrated under reduced pressure yielding white crystals (0.630 g, 3.07 mmol, 20.5%). ^{1}H NMR ($CDCl_3$): δ 6.98 (m, 8H); 5.45 (m, 1H). ^{13}C NMR ($CDCl_3$): δ 157.78; 139.76; 119.46; 116.07. ^{19}F NMR ($CDCl_3$): δ −122.67 (p, 2F). HRMS: m/z calcd for $C_{12}H_9F_2N$ $[M+H]^+$: 206.0776. Found: 206.0782 (3.09 ppm).

4-Fluoro-N-(4-fluorophenyl)-N-2-propen-1ylbenzenamine. To a clean Schlenk flask (200 mL) was added 4-fluoro-*N*-(4-fluorophenyl)-benzenamine (0.509 g, 2.5 mmol) and sodium *tert*-butoxide (0.246 g, 3.0 mmol) in a glovebox. The flask was connected to a Schlenk line, and distilled tetrahydrofuran was added via syringe. While the reaction mixture was stirring, allylbromide (0.26 mL, 3.0 mmol) was added dropwise by syringe. The reaction mixture was then refluxed under an N_2 atmosphere for 12 h. The reaction mixture was concentrated at reduced pressure and purified by silica gel column chromatography with hexane. The first band was collected, concentrated at reduced pressure, and determined to be the product (0.425 g, 1.73 mmol, 69.3%). ^{1}H NMR ($CDCl_3$): δ 6.96 (m, 8H); 5.92 (m, 1H); 5.21 (m, 2H); 4.25 (m, 2H). ^{13}C NMR ($CDCl_3$): δ 157.89; 144.33; 133.98; 122.01; 116.73; 115.74; 55.38. ^{19}F NMR ($CDCl_3$): δ −122.50 (m, 2F). HRMS: m/z calcd for $C_{15}H_{14}F_2N$ $[M+H]^+$: 246.1089. Found 246.1087 (0.6 ppm). EA calcd for $C_{15}H_{13}F_2N$: C, 73.45; H, 5.34; F, 15.49; N, 5.71. Found: C, 73.97; H, 5.21; F, 15.1; N, 5.67.

N-(3-Trichlorosilylpropyl)-4-fluoro-N-(4-fluorophenyl)-benzenamine (F_2PAPTSi). To a clean and dried Schlenk storage flask (20 mL) was added 4-fluoro-*N*-(4-fluorophenyl)-*N*-2-propen-1ylbenzenamine (0.262 g, 1.07 mmol) and trichlorosilane (1.0 mL, 9.9 mmol), and a catalytic amount of chloroplatinic acid hydrate. Distilled dichloromethane (10 mL) was then added.[6] The solution was stirred at room temperature for 24 h and then filtered and transferred to another clean and dried Schlenk flask (20 mL) with a 0.22 μm PTFE syringe filter. The flask was then placed under reduced pressure to remove the solvent and remaining trichlorosilane, and then heated at 50 °C under a flowing N_2 atmosphere for 2 h to evaporate any other impurities. The product was a pale yellow oil (0.255, 0.67 mmol, 62.6%). Anhydrous toluene (10 mL) was added to the flask to make a 25 mg/mL solution for a further use. ^{1}H NMR ($CDCl_3$): δ 6.95 (m, 8H); 3.65 (t, 2H); 1.90 (p, 2H); 1.43 (m, 2H). ^{13}C NMR ($CDCl_3$): δ 158.23; 144.31; 122.15; 115.93; 54.27; 21.71; 20.51. ^{19}F NMR ($CDCl_3$): δ −121.76 (m, 2F).

3,4-Difluoro-N-(3,4-difluorophenyl)-benzenamine. To a clean and dried Schlenk flask (200 mL) were added tris[dibenzylideneacetone]-dipalladium(0) (0.4163 g, 3.0 mol %), tri(*tert*-butyl)phosphine (0.090 g, 3.0 mol %), and sodium *tert*-butoxide (1.7414 g, 18.1 mmol) in a glovebox.[55] The flask was connected to a Schlenk line, and then anhydrous hexane (80 mL) was added. 3,4-Difluoro-1-benzenamine (1.5 mL, 15.1 mmol) and 1-bromo-3,4-difluorobenzenamine (1.7 mL, 15.0 mmol) were added. The reaction mixture was stirred at 60 °C overnight, and then cooled to room temperature. The product was purified by silica gel chromatography, eluting with hexane. The first

band was collected and concentrated under reduced pressure yielding white crystals (1.61 g, 6.68 mmol, 44.2%). ^{1}H NMR ($CDCl_3$): δ 7.04 (m, 2H); 6.89 (m, 2H); 6.73 (m, 2H); 5.58 (s, 1H). ^{13}C NMR ($CDCl_3$): δ 150.73; 145.53; 139.52; 117.94; 113.81; 107.25. ^{19}F NMR ($CDCl_3$): δ −135.74 (p, 2F); −146.46 (m, 2F). HRMS *m/z* calcd for $C_{12}H_6F_4N$ $[M-H]^-$: 240.0442. Found: 240.0449 (−3.04 ppm).

3,4-Difluoro-N-(3,4-difluorophenyl)-N-2-propen-1-ylbenzenamine. To a clean Schlenk flask (200 mL), 3,4-difluoro-N-(3,4-difluorophenyl)-benzenamine (0.300 g, 1.24 mmol) and sodium *tert*-butoxide (0.146 g, 1.5 mmol) were added in a glovebox. The flask was connected to a Schlenk line, and distilled tetrahydrofuran was added via syringe. While the reaction mixture was stirring, allylbromide (0.13 mL, 1.5 mmol) was added dropwise by syringe. The reaction mixture was refluxed under an N_2 atmosphere for 12 h. The reaction mixture was concentrated at reduced pressure, and then purified by silica gel column chromatography, eluting with hexane. The first band was collected, concentrated under reduced pressure, and determined to be the product (0.344 g, 1.2 mmol, 98.6%). ^{1}H NMR ($CDCl_3$): δ 7.08 (m, 2H); 6.82 (m, 2H); 6.72 (m, 2H); 5.90 (m, 2H); 5.23 (m, 2H); 4.24 (d, 2H); ^{13}C NMR ($CDCl_3$): δ 150.39; 145.42; 144.78; 133.06; 117.72; 117.28; 116.43; 109.93; 55.29; ^{19}F NMR ($CDCl_3$): δ −135.70 (p, 2F); −146.17 (m, 2F). HRMS: *m/z* calcd for $C_{15}H_{11}F_4N$ $[M]^+$: 281.0828. Found: 281.0829 (0.4 ppm). EA calcd for $C_{15}H_{11}F_4N$: C, 64.06; H, 3.94; F, 27.02; N, 4.98. Found: C, 64.39; H, 4.08; F, 27.14; N, 5.05.

N-(3-Trichlorosilylpropyl)-3,4-difluoro-N-(3,4-difluorophenyl)-benzenamine (F_4PAPTSi). To a clean and dried Schlenk storage flask (20 mL) was added 3,4-difluoro-N-(3,4-difluorophenyl)-N-2-propen-1-ylbenzenamine (0.095 g, 0.39 mmol) and trichlorosilane (0.5 mL, 5.0 mmol), and a catalytic amount of chloroplatinic acid hydrate. Distilled toluene (5 mL) was added.[6] The solution was stirred at room temperature for 24 h and then filtered and transferred to another clean and dried Schlenk flask (20 mL) with a 0.22 μm PTFE syringe filter. The flask placed under reduced pressure to remove the solvent and remaining trichlorosilane, and then heated to 50 °C under flowing N_2 for 2 h to evaporate impurities. The product was a slightly yellow oil (0.050, 0.12 mmol, 30.8%). Anhydrous toluene (9.5 mL) was added to the flask to make a 25 mg/mL solution for the further use. ^{1}H NMR ($CDCl_3$): δ 7.08 (m, 2H); 6.73 (m, 2H); 6.65 (d, 2H); 3.63 (t, 2H); 1.85 (p, 2H); 1.42 (m, 2H). ^{13}C NMR ($CDCl_3$): δ 150.82; 146.13; 144.18; 118.06; 116.89; 110.39; 54.40; 21.59; 20.48. ^{19}F NMR ($CDCl_3$): δ −135.20 (m, 2F); −145.49 (m, 2F).

3,4,5-Trifluoro-N-(3,4,5-trifluorophenyl)-benzenamine. To a clean and dried Schlenk flask (200 mL) was added tris[dibenzylideneacetone]dipalladium(0) (0.419 g, 3.0 mol %), tri(*tert*-butyl)-phosphine (0.0898 g, 3.0 mol %), and sodium *tert*-butoxide (1.7336 g, 18 mmol)in a glovebox.[55] The flask was connected to a Schlenk line, and then anhydrous hexane (80 mL) was added. Next, 3,4,5-trifluoro-1-benzenamine (2.212 g, 15 mmol) from Alfa Aesar and 5-bromo-1,2,3-trifluorobenze (1.77 mL, 15 mmol) from TCI America were also added without further purification. The reaction mixture was stirred at 60 °C overnight, and then cooled to room temperature. The product was purified by silica gel chromatography, eluting with hexane. The first band was collected and concentrated under reduced pressure yielding white crystals (1.63 g, 5.88 mmol, 39.2%). ^{1}H NMR ($CDCl_3$): δ 6.68 (m, 4H); 5.79 (s, 1H). ^{13}C NMR ($CDCl_3$): δ 151.88; 137.81; 135.24; 102.43. ^{19}F NMR ($CDCl_3$): δ −132.82 (dd, 4F); −168.38 (tt, 2F). HRMS: *m/z* calcd for $C_{12}H_4F_6N$ $[M-H]^-$: 276.0253. Found: 276.0260 (−2.43 ppm).

3,4,5-Trifluoro-N-(3,4,5-trifluorophenyl)-N-3-propen-1-ylbenzenamine. To a clean Schlenk flask (200 mL) was added 3,4,5-trifluoro-N-(3,4,5-trifluorophenyl)-benzenamine (0.686 g, 2.5 mmol) and sodium *tert*-butoxide (0.251 g, 3.0 mmol) in a glovebox. The flask was connected to a Schlenk line, and anhydrous THF was added via syringe. While the reaction mixture was stirring, allylbromide (0.26 mL, 3.0 mmol) was added dropwise by a syringe. The reaction mixture was then refluxed under N_2 for 12 h. The reaction mixture was concentrated at reduced pressure, then purified by silica gel column chromatography, eluting with hexane. The first band was collected, concentrated at reduced pressure, and determined to be the product (0.6801 g, 2.1 mmol, 85.6%). ^{1}H NMR ($CDCl_3$): δ 6.63 (m, 4H); 5.84 (m, 2H); 5.25 (m, 2H); 4.23 (d, 2H). ^{13}C NMR ($CDCl_3$): δ 151.71; 142.37; 135.56; 132.20; 117.82; 105.14; 55.16. ^{19}F NMR ($CDCl_3$): δ −132.98 (dd, 4F); −167.95 (tt, 2F); HRMS *m/z* calcd for $C_{15}H_9F_6N$ $[M]^-$: 317.0639. Found 317.0636 (−0.9 ppm). EA calcd for $C_{15}H_9F_6N$: C, 56.79; H, 2.86; F, 35.93; N, 4.42. Found: C, 58.28; H, 3.13; F, 33.61; N, 5.02.

N-(3-Trichlorosilylpropyl)-3,4,5-trifluorophenyl-N-(3,4,5-trifluorophenyl)-benzenamine (F_6PAPTSi). To a clean and dried Schlenk storage flask (20 mL) were added 3,4,5-trifluoro-*N*-(3,4,5-trifluorophenyl)-*N*-3-propen-1-ylbenzenamine (0.2722 g, 0.86 mmol) and trichlorosilane (1.0 mL, 9.9 mmol), and a catalytic amount of chloroplatinic acid hydrate. Distilled toluene (10 mL) was added.[6] The solution was stirred at room temperature for 24 h, and then the solution was filtered and transferred to another clean and dried Schlenk flask (20 mL) with a 0.22 μm PTFE syringe filter. The flask placed under reduced pressure to remove the solvent and remaining trichlorosilane, and then heated to 50 °C under flowing N_2 for 2 h to evaporate any other impurities. The product was a slightly yellow oil (0.2949, 0.65 mmol, 75.8%). Anhydrous toluene (11.8 mL) was added to the flask to make a 25 mg/mL solution for the further use. ^{1}H NMR ($CDCl_3$): δ 6.55 (m. 4H); 3.66 (t, 2H); 1.93 (p, 2H); 1.44 (m, 2H); ^{13}C NMR ($CDCl_3$): δ 152.05; 142.37; 135.93; 105.48; 54.14; 21.47; 20.47; ^{19}F NMR ($CDCl_3$): δ −132.36 (dd, 4F); −167.17 (tt, 2F).

2,3,4,5,6-pentafluoro-N-(2,3,4,5,6-pentafluorophenyl)-benzenamine. To a clean, dried Schlenk flask (100 mL) was added lithium amide (1.12 g, 48.8 mmol) from Alfa Aesar and distilled THF (25 mL) was added under a N_2 atmosphere. The flask was then cooled to 15 °C in an acetone bath, and hexafluorobenzene (8.7 g, 47.8 mmol) from Alfa Aesar was added to the flask.[56] The solution was next refluxed for 2 h while stirring, then cooled to 0 °C by an ice bath. The solution was diluted with ethyl ether (25 mL) then 5% aqueous hydrochloric acid was added to hydrolyze the product. Saturated aqueous ammonium chloride was added and the solution was stirred for 30 min. The organic layer was separated, and the aqueous layer was washed with ethyl ether (3 × 30 mL). The ethyl ether layer was combined with the previously separated organic layer, the solution dried over anhydrous $MgSO_4$, filtered, and then the solvent was removed under reduced pressure. A silica gel flash column chromatography was performed, eluting with hexane, and the first band was collected. The solvent was removed under reduced pressure, yielding a white crystalline solid (3.20g, 9.17 mmol 19.1%). ^{1}H NMR ($CDCl_3$): δ 5.23 (s, 1H). ^{13}C NMR ($CDCl_3$): δ 141.53; 137.88; 137.21; 117.15. ^{19}F NMR ($CDCl_3$): δ −153.91 (dd, 4F); −162.70 (m, 6F). HRMS *m/z* calcd for $C_{12}F_{10}N$ $[M-H]^-$: 347.9877. Found 347.9890 (−3.74 ppm).

2,3,4,5,6-Pentafuloro-N-(2,3,4,5,6-pentafluorophenyl)-N-2-propen-1-ylbenzenamine. To a clean and dried Schlenk flask (25 mL) were added 2,3,4,5,6-pentafluoro-*N*-(2,3,4,5,6-pentafluorophenyl)-benzenamine (2.14 g, 6.13 mmol), K_2CO_3 (1.72 g, 12.4 mmol), 1-bromo-3-propene (10.8 mL, 143 mmol), tetrabutylammonium iodide (0.120 g, 0.324 mmol), and acetonitrile (4.5 mL).[54] The solution was then refluxed at 84 °C for 17 h while stirring, and then cooled to room temperature. The solution was diluted with deionized water (10 mL), and the product was extracted with ethyl acetate (3 × 15 mL). The organic layers were combined and dried over anhydrous $MgSO_4$. The organic layer was concentrated under reduced pressure, and the product was purified by silica gel column chromatography with hexane as the eluent. The first band was collected and determined to be the product, colorless crystals (2.05 g, 5.27 mmol, 86.0%). ^{1}H NMR ($CDCl_3$): δ 5.95 (m, 1H); 5.21 (dd, 2H); 4.2 (d, 2H). ^{13}C NMR ($CDCl_3$): δ 145.12; 138.89; 137.92; 132.72; 120.80; 67.47; 30.98; ^{19}F NMR ($CDCl_3$): δ −148.24 (d, 4F); −159.19 (t, 2F); −162.52 (m, 4F). HRMS: *m/z* calcd for $C_{15}H_5F_{10}N$ $[M]^+$: 389.0262. Found: 389.0268 (1.5 ppm). EA calcd for $C_{15}H_5F_{10}N$: C, 46.29; H, 1.29; F, 48.82; N, 3.60. Found: C, 46.23; H, 1.41; F, 48.63; N, 3.56.

N-3-(trichlorosilylpropyl)-2,3,4,5,6-pentafluoro-N-(2,3,4,5,6-pentafluorophenyl)-benzenamine (F_{10}PAPTSi). To a clean and dried Schlenk storage flask (20 mL) was added 2,3,4,5,6-pentafuloro-*N*-(2,3,4,5,6-pentafluorophenyl)-*N*-2-propen-1-ylbenzenamine (0.524 mg, 1.35 mmol) and trichlorosilane (1.0 mL, 9.9 mmol), and a

catalytic amount of chloroplatinic acid hydrate were added. Distilled toluene (10 mL) was added.[6] The solution was stirred at room temperature for 24 h, and the solution was then filtered and transferred to another clean, dry Schlenk flask (20 mL) through a 0.22 μm PTFE syringe filter. The flask placed under reduced pressure to remove the solvent and remaining trichlorosilane, and then heated to 50 °C under a flowing N_2 atmosphere for 2 h to evaporate any other impurities. The product was a slightly yellow oil (0.626, 1.19 mmol, 88.4%). Anhydrous toluene (12.3 mL) was added to the flask to make a 50 mg/mL solution for the further use. ^{1}H NMR ($CDCl_3$): δ 3.67 (t, 2H); 1.85 (p, 2H); 1.45 (t, 2H). ^{13}C NMR ($CDCl_3$): δ 144.48; 139.40; 138.24; 121.05; 55.84; 21.55; 20.96. ^{19}F NMR ($CDCl_3$): δ −148.18; −158.21; −161.87.

Computational Analysis. Optimized geometries, HOMO and LUMO energy levels, planarity at the N centers, and the dimensions of the SAM precursors were analyzed by DFT methods using the Radon cluster of Northwestern University.[57−62] The Becke 3 parameter functional combined with the Lee, Yang, and Parr (B3LYP) gradient-corrected method,[63−66] and Pople's 6-311G(d) split valence[67] were used as the basis set for the computational software package GÅMESS version 12 JAN 2009 (R2) from the Gordon research group at Iowa State U.,[68] and the results were cross-checked with another software package, Q-Chem version 4.01 from Q-Chem, Inc.[69] The optimized molecular geometries were visualized by MacMolPlt version 7.4.2.[70] To reduce computational demands, the $-SiCl_3$ moiety was replaced with a H atom. The molecular geometry was optimized from a simpler basis set first, then advanced to a more elaborate basis set for a greater accuracy. The atomic coordinates of the optimized molecular geometry were then used for the Hessian input, and the molecular energy levels and dipole moments were obtained.

B. Interfacial Layer Characterization. The SAM-modified and air-plasma-treated Si(100)/SiO_2 or glass/ITO substrates were characterized by contact angle (CA) measurements, atomic force microscopy (AFM), X-ray reflectivity (XRR), ultraviolet photoelectron spectroscopy (UPS), X-ray photoelectron spectroscopy (XPS), grazing incidence X-ray diffraction (GIXD), and cyclic voltammetry (CV).

Interfacial Layer Deposition. IFLs were grafted onto Si(100)/SiO_2 wafers and glass/ITO substrates under a N_2 atmosphere. Si(100) wafers with 3000 Å of thermally grown SiO_2 were obtained from WRS Materials, and patterned glass/ITO substrates with an ITO thickness of 280 nm and a resistivity of <10 mΩ were purchased from Thin Film Devices, Inc. The Si(100)/SiO_2 substrates were first cleaned by sonicating in ethanol (2x 200 grade), followed by air plasma (AP) cleaning (1 min at 400 mTorr). The ITO substrates were cleaned in hexane, detergent, deionized water, methanol, isopropanol, and acetone, respectively, for 30 min each at 50 °C. The substrates were subsequently cleaned in an AP cleaner (1 min at 400 mTorr) and then quickly transferred to an inert atmosphere deposition chamber. For AP treated devices, the substrates were transferred to a glovebox immediately at this stage. Solutions of **F_nPAPTSi** were prepared in anhydrous toluene at concentrations of 0.50, 0.10, and 0.026 mM and transferred to the deposition chamber using Schlenk protocol. The substrates were then immersed in the **F_nPAPTSi** solution for 5 h, 14 h, or 17 h at room temperature. The surface roughnesses of the coatings were monitored by AFM and the approximate IFL packing density was monitored by CA measurements. For the OPV device fabrication, optimum conditions were chosen for the SAM/IFL growth namely, 0.025 mM precursor solution deposited for 24 h at room temperature under inert atmosphere. The modified substrates were washed with anhydrous toluene (3×), then immersed in ethanol (200 grade) and sonicated for 1 min to remove any physisorbed species and to quench unreacted chlorosilane moieties. For PEDOT:PSS film deposition, a UV/O_3 oven (20 min) was used instead of an AP cleaner to clean the substrates, and the aqueous PEDOT:PSS solution (Clevios P VP Al 4083, 1:6 wt ratio) was filtered through a syringe filter (0.20 μm) and spin-coated onto cleaned ITO substrates at 5000 rpm for 30 s (~40 nm film thickness). The films were then annealed at 150 °C for 15 min under ambient before transferring to a glovebox. Each type of substrate is named: **F0-**, **F2-**, **F4-**, **F6-**, **F10-**, **bare**, and **PEDOT:PSS-Si** or **ITO** for Si(100)/SiO_2 or glass/ITO substrates modified with **F_0PAPTSi**, **F_2PAPTSi**, **F_4PAPTSi**, **F_6PAPTSi**, **F_{10}PAPTSi**, AP-treated, or coated with PEDOT:PSS, respectively.

CA Measurements. Equilibrium contact angles on the IFL-modified glass/ITO substrates were measured using a VCA Optima (AST Products) goniometer by placing a 2 μL droplet on the substrate surface. After 30 s, a droplet image was obtained, which was fitted using the manufacturer's software. The recorded contact angle was determined by averaging measurements from both sides of the droplet. Substrate surface energy was calculated using the geometric mean model[71] with diiodomethane (γ^d = 48.5 mJ/m^2, γ^p = 2.3 mJ/m^2) and water (γ^d = 21.8 mJ/m^2, γ^p = 51.0 mJ/m^2) as probe liquids.[72] Further details regarding the processed experimental data are included in the Supporting Information.

AFM Analysis. A Bruker ICON PT system was used to characterize Si(100)/SiO_2, glass/ITO, and **Fn-ITO** surface morphologies. Images were recorded using the ambient tapping mode with Applied NanoStructures ACTA N-type Si cantilevers with a < 10 nm tip radius curvature. Several locations of the **Fn-ITO** substrates were examined with a scan area of 1 × 1 μm or 0.5 × 0.5 μm to ensure reproducibility. All height images obtained were leveled prior to the r.m.s. roughness measurement.

X-ray Reflectivity. XRR data from the modified Si(100)/SiO_2 substrates were acquired using an 18 kW Rigaku ATXG workstation at Northwestern University's J.B Cohen X-ray facility. CuKα radiation (wavelength λ = 1.542 Å) was conditioned by a parabolic multilayer mirror and collimated to produce a 0.1 mm (vertical) by 5 mm (horizontal) beam with an incident flux of ~1 × 10^8 photons/s. The X-ray reflectivity data are plotted as a function of the momentum transfer vector with modulus, $q = 4\pi \sin(2\theta/2)/\lambda$, where the 2θ is the scattering angle. The fitted data were processed following the method of Fukuto et al.[73] to obtain the film thickness and electron density.

UPS Measurements. A Kratos Axis Ultra photoelectron spectrometer with a base pressure of 2 × 10^{-9} Torr was used for ultraviolet photoelectron spectroscopy (UPS) and X-ray photoelectron spectroscopy (XPS) studies. For UPS, a He I photon source (21.22 eV) with a pass energy of 5 eV and a 20 mA emission current was used. To identify the secondary electron cutoff (SECO), a sample bias of −10.0 V was applied to increase the vacuum level of the sample relative to that of the spectrometer. The SECO was determined from each spectrum by fitting a line to the leading 80% of the data points. The data presented here are plotted with the Fermi edge set at 0.0 eV, and the work function was calculated by subtracting SECO from the photon energy. The instrument was calibrated such that in situ cleaned (Ar^+ sputtered) gold foil had a work function of 5.1 eV and Fermi edge at 0.0 eV.

XPS Measurements. XPS measurements on the modified glass/ITO substrates were made with a monochromatic Al source (1486.6 eV) and pass energy of 160 eV over a range of 0−1200 eV. The emission current was fixed at 10 mA with a 12 kV operating voltage. Spectra were collected by averaging 5 sweeps with a step size of 1 eV and a 100 ms dwell time. Elemental analysis was performed by fitting collected spectra with Gaussian−Lorentzian line shapes after subtracting Shirley backgrounds. Due to overlap between the F 1s peak and the loss feature of the In $3p_{3/2}$ band, the fluorine content of the modified SAMs was determined after subtracting the unmodified **F0-ITO** spectra to remove the associated In $3p_{3/2}$ loss structure. Sample charging was compensated by offsetting the spectra so that the C 1s peak was fixed at 284.5 eV.

Grazing Incidence X-ray Diffraction. These measurements on **F4-**, **F6-**, and **F10-ITO** substrates were performed at Beamline 8ID of the Advanced Photon Source (APS) at Argonne National Laboratory. Scattering intensities are expressed as a function of the scattering vector, $q = 4\pi/\lambda\sin(\theta)$, where θ is the half of the scattering angle and λ = 1.6868 Å is the wavelength of incident radiation. A Pilatus detector was used to collect the scattering images and was situated at 203 mm from the sample for the GIXD measurements. The films were illuminated at incidence angles 0.1−0.7° by 7.35 keV X-rays in order to illuminate the SAM structure while minimizing background scattering. Exposure times were varied from 1 to 30 s.

Scheme 1. Synthetic Routes to F_nPAPTSi SAM-IFL Precursors[a]

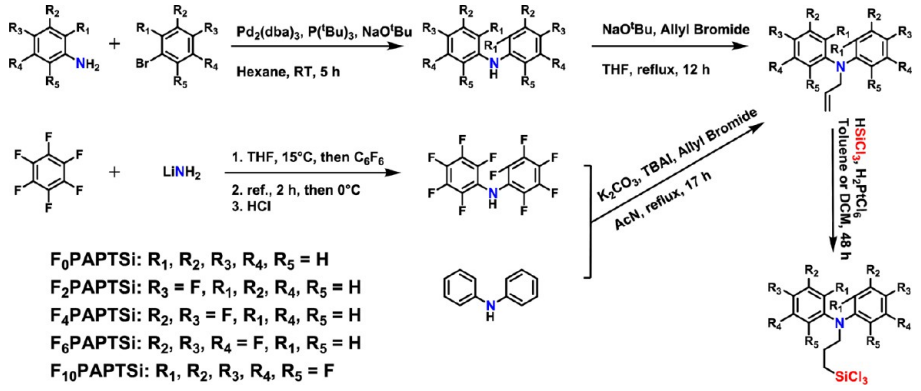

[a]Here, *n* denotes the number of F atoms on the aryl rings.

Cyclic Voltammetry. The oxidation potentials of the IFL precursors and heterogeneous electron transport rate constants were calculated from CV data. The CV data were obtained by EC epsilon potentiostat with C-3 cell stand from BASi. For oxidation potential measurements, electrolyte solutions of recrystallized $(n\text{-}Bu_4)N^+PF_6^-$ in anhydrous acetonitrile (0.1 M) were prepared and used for the analysis, with a Pt working electrode, Pt counter electrode, and a Ag pseudo reference electrode with a ferrocenium/ferrocene (Fc^+/Fc) internal standard[74] were used for measurements. A few drops of the **F_nPAPTSi** solution were placed on the Pt working electrode by syringe. The solvent was evaporated while promoting cross-linking under ambient conditions until the surface of the working electrode was completely covered. The electrode was then submerged in the electrolyte solution and equilibrated for 10 s before the scan was started. All data were calibrated with the ferrocene half peak ($Fc_{1/2}$), the average of the oxidation and the reduction (Fc^+/Fc) onsets. The analyte was scanned at 100 mV/s scan rate and a sweep range of 3000 mV to −1200 mV. For the direct heterogeneous electron transport rate constant measurements, the IFL-coated ITO substrates were used as the working electrode, with a Pt counter electrode, and a Ag pseudo reference electrode, and $Fc_{1/2}$ calibration. Scan rates from 0.1 V/s to 25.0 V/s and a sweep range of 2300 mV to 0 mV were used in an electrolyte of 0.1 M $(n\text{-}Bu_4)N^+PF_6^-$ in anhydrous acetonitrile, and the shifts in the oxidation and reduction onset potentials of Fc were recorded. For the indirect heterogeneous electron transport rate constant measurements, the IFL-coated ITO substrates were used as the working electrode, with a Pt counter electrode, and a Ag pseudo reference electrode, and $Fc_{1/2}$ calibration. Scan rates from 50 to 1600 mV/s and a sweep range of 1000 to −200 mV were used with a 0.1 M $(n\text{-}Bu_4)N^+PF_6^-$ electrolyte and 0.002 M Fc as the probe species in anhydrous acetonitrile, and the shifts in the oxidation and reduction onset potentials of Fc were recorded.

OPV Fabrication. Well-stirred dispersions of a poly(3-hexylthiophene):phenyl-C_{71}-butyric acid methyl ester (P3HT:$PC_{71}BM$) blend in dry *o*-DCB (1:1 by wt., 20 mg/1 mL ea.) and a poly[[4,8-bis[(2-ethylhexyl)oxy]benzo[1,2-b:4,5-b']dithiophene-2,6-diyl][3-fluoro-2-[(2-ethylhexyl)carbonyl]thieno[3,4-b]thiophenediyl]] (PTB7) and $PC_{71}BM$ blend (PTB7:$PC_{71}BM$) in dry CB (2:3 by wt., 10 mg/1 mL ea.) were prepared. P3HT, PTB7, and PC71BM were obtained from Rieke Metals, 1 Materials, and American Dye Source, respectively. The P3HT:$PC_{71}BM$ solution was stirred for 12 h at 70 °C under a N_2 atmosphere, and the PTB7:$PC_{71}BM$ solution was stirred for 24 h at 70 °C; then 1,8-diiodooctane (3% v/v) was added to the PTB7:$PC_{71}BM$ solution with stirring for 1 h at 70 °C under a N_2 atmosphere. The P3HT:$PC_{71}BM$ solution was next filtered through a syringe filter (0.22 μm) and spin-coated (1 min at 550 rpm, then 1 s at 2000 rpm) onto the **Fn-**, bare, and **PEDOT:PSS-ITO** substrates and slow-dried in Petri dishes. The PTB7:$PC_{71}BM$ solution was spin-coated (30 s at 2000 rpm) in a similar manner. The P3HT:$PC_{71}BM$ coated substrates were next annealed at 120 °C for 10 min. LiF (1 nm, 0.1 nm/s) and Al (130 nm, 1.5 nm/s) were then deposited by vacuum deposition with a shadow mask to yield 4 device pixels (0.2 cm × 0.35 cm, device area = 0.07 cm^2 each). All devices were encapsulated using a cover glass sealed with UV-curable epoxy, cured by UV radiation for 10 min.

OPV Characterization. A Spectra-Nova Class A Solar Simulator with AM1.5G light (100 mW/cm^2) from a 500 W Xe arc lamp was used to characterize OPV devices. All OPV devices were masked with an aperture of a device pixel dimension. The light source was calibrated with an NREL-certified Si diode equipped with a KG3 filter to bring spectral mismatch to unity. The *J*−*V* curve data were obtained from a Keithly 2400 digital source meter. External quantum efficiency (EQE) was measured by an Oriel Model QE−PV-SI instrument (Newport Instruments) equipped with a NIST-certified Si-diode, a Merlin lock-in amplifier, and an optical chopper. Monochromatic light was generated from a 300 W Xe arc lamp. The integrated external quantum efficiency (EQE) data were found to be in good agreement with the measured short circuit current (J_{sc}) data.

RESULTS

In this section, the syntheses and structures of the new SAM-IFL precursors are first described, followed by their chemisorption properties. The characterization of the **Fn-ITO** and **Fn-Si** SAMs/IFLs is then presented, providing information on surface energy, surface morphology, elemental composition, SAM thickness, SAM packing density, and SAM crystallinity. The electronic structures and related properties of the **Fn-ITO** anodes are then extracted with computational modeling and the experimental data. Finally, the photovoltaic response systematics of BHJ OPVs fabricated using two different donor−acceptor active layer systems and the modified ITO anodes are presented and discussed in relationship to trends in the IFL properties.

A. Interfacial Layer Precursor Synthesis and Characterization. The **F_nPAPTSi** IFL precursor reagents, the diarylamine cores, and the corresponding diarylallylamines, were synthesized via the pathways shown in Scheme 1 and purified by silica gel column chromatography. The structure and purity of each diarylallylamine intermediate was confirmed by ^1H, ^{13}C, and ^{19}F NMR coupled with HRMS and C, H, N elemental analyses, and the purity was determined to be >95%. After hydrosilylation (Scheme 1) the **F_nPAPTSi** compounds were also characterized by ^1H, ^{13}C, and ^{19}F NMR spectroscopy, and their isomeric purity was determined to be ≥70% with the majority of the impurities assigned to not unexpected C═C isomerization or hydrogenation byproducts.[75] Upon warming the product oils under an N_2 flow at 50 °C for 0.5 to 2.0 h to volatize the lower boiling contaminants, the purity was

dx.doi.org/10.1021/am4030609 | ACS Appl. Mater. Interfaces 2013, 5, 9224−9240

enhanced to ≥80% by ^{1}H NMR analysis. Note that further purification by recrystallization or column chromatography was not possible due to the oily character of the products and highly reactive nature of the $-SiCl_3$ moieties. The ^{1}H, ^{13}C, and ^{19}F NMR spectra of all new compounds are provided in the Supporting Information.

B. Surface Physicochemical Properties. *SAM Growth Optimization.* The course of formation of densely packed smooth films was monitored by ambient tapping mode AFM height images and advancing aqueous contact angle (CA) measurements. The concentration of the **F_{10}PAPTSi**, the SAM-IFL precursor, solution was reduced from 0.50 mM to 0.026 mM until no noticeable island formation was observed on modified Si(100)/SiO_2 substrates. The surface roughness (R_q) was compared to the native surface roughness of Si(100)/SiO_2 substrates (0.117 nm), and 0.50 mM, 0.10 mM, and 0.026 mM precursor solutions yielded R_q = 0.622, 0.193, and 0.176 nm, respectively. A final sonication in ethanol was found to be critical for removing any remaining physisorbed material and quenching unreacted Cl−Si moieties, and therefore to obtaining low roughness values. The R_q values from the AFM measurements were found to be comparable to those obtained from the XRR analysis (~0.24 nm).

The SAM-IFL precursor solutions used in this study were significantly more dilute than those used in previous OLED IFL studies (1.0 mM).[4,10] However, the immersion time in the present work was varied from 5 to 17 h to monitor coverage and ensure saturation of the **F_0PAPTSi** SAM coverage on the glass/ITO substrates by aqueous CA measurements. After 5 h, the advancing aqueous CA of the **F0-ITO** substrate is 52°, increases to 84° after 14 h immersion, and then remains constant (82°) after 17 h immersion. This CA is comparable to other structurally similar densely packed SAM-modified substrates (85°).[76] As discussed by Terrill et al.,[77] longer immersion times typically lead to SAM density saturation. Thus, to achieve the maximum SAM density for all precursors used in this study, 24 h immersion times were used as the standard. A summary of results and AFM images are included in the Supporting Information (S2).

Advancing Contact Angles. The surface energies of the plasma-treated bare ITO and **Fn-ITO** substrates were extrapolated from contact angle measurements using diiodomethane and water as probe liquids[72] in conjunction with a geometric mean model. This model describes the total adhesion energy W_{adh} deduced from the total liquid surface energy γ_l^T, which in turn is related to the dispersive (γ_i^d) and polar surface energy components (γ_i^p) of both the substrate and probe liquid (subscripts s and l) as in eq 1.[71]

$$W_{adh} = \gamma_l^T(1 + \cos\theta) = 2(\sqrt{\gamma_s^d\gamma_l^d} + \sqrt{\gamma_s^p\gamma_l^p}) \quad (1)$$

The derived surface energies (Figure 4) are reduced by roughly 50% from the total glass/ITO surface energy upon grafting **F_nPAPTSi** onto the glass/ITO substrate. The dispersive nature of the **Fn-ITO** surfaces remains relatively unchanged, whereas the polar component of the SAM covered substrates falls appreciably. In particular, an apparent decrease of the **F10-ITO** dispersive component is observed at high F contents. This phenomenon is not unexpected since the surface has been converted from a hydroxyl-coated hydrophilic surface to fluoroaryl- or aryl-coated hydrophobic surface. When compared with **PEDOT:PSS** (γ^d = 40.6 mJ/m^2, γ^p = 30.6 mJ/m^2),[78] a significant reduction in the polar component should oppose

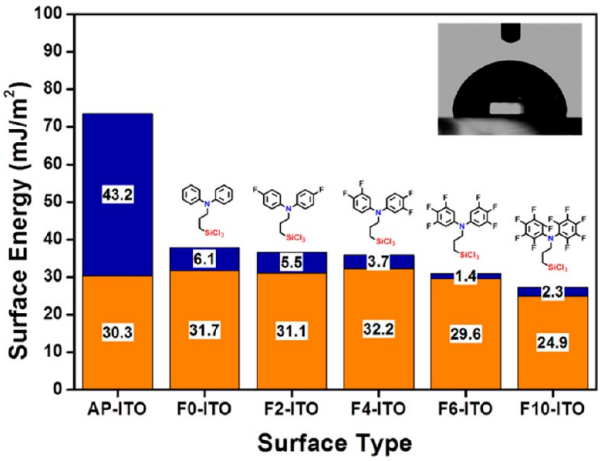

Figure 4. Contact angle data for glass/ITO substrates coated with the various IFLs. The image at the upper right is a water droplet on an **F4-ITO** surface. Blue bars denote the polar component, and orange bars denote the dispersive component of the respective surface. The sum of the polar and nonpolar components is the total surface energy.

delamination of the active layer polymer films due to the reduction in the surface energy mismatch.[4,8,18,43,79] Similar trends have been reported in the literature for SAMs derived from analogous precursors.[76] Contact angle data are tabulated in the Supporting Information (S3).

X-ray Reflectivity. SAM-IFL thickness, surface roughness, and packing density on Si(100)/SiO_2 substrates, reasonably assumed to be similar to those on glass/ITO substrates, were characterized by X-ray reflectivity (XRR; Table 1). The XRR data can be fit to a single-slab model representing a single organic film layer on the Si(100)/SiO_2 substrate (Figure 5). For **F_nPAPTSi** structures (Figure 2), film thicknesses of roughly 8−11 Å are anticipated assuming the molecules pack vertically in dense monolayers. The derived SAM-IFL film thicknesses from this analysis range from 6.7 to 9.7 Å. A film thicknesses less than the molecular length implies molecular tilting away from the surface normal. With the exception of **F0−Si**, the derived thicknesses correspond well with expectation, allowing for some molecular tilting. Surface roughnesses were extracted by fitting the theoretical parameters to the experimental data. The packing density (Γ), or surface coverage, was calculated from the electron density (d_e),[10] and the film electron density (N_{film}) was calculated by multiplying d_e by the thickness. The total number of valence electrons of a precursor molecule was calculated (N_{mol}) and divided by N_{film} yielding the molecular footprint in Å^2. The inverse of the molecular footprint is used to derive Γ (Table 1). All of these IFLs have a molecular coverages ranging from 2.5 to 3.8 × 10^{-10} mol cm^{-2}, suggesting near maximum packing density. Assuming 4.9 −OH moieties/nm^2 on the SiO_2 surface[80] and that only one −OH unit is needed for SAM precursor covalent attachment, ~4.9 precursor molecules can presumably bind/nm^2 of the SiO_2 surface. Taking into account the approximate molecular "footprint" estimated from the DFT-calculated optimized geometry (e.g., 4.82 Å x 10.1 Å for the **F_4PAPTSi**; see the Supporting Information S6), the maximum achievable molecular density is ~2.1 molecules nm^{-2} or 3.3 × 10^{-10} mol cm^{-2}. Therefore, it can be concluded that **F_nPAPTSi** molecules form densely packed monolayers on the Si(100)/SiO_2 surface and likely on the glass/ITO surface as well.

Table 1. Computed and Measured Properties of the Indicated IFLs Chemisorbed on ITO or Si/SiO_2

IFL	Φ_s[a] (eV)	VBM[a] (eV)	μ_z[b,d] (debye)	tilt[b,e] (deg)	thickness[b] (Å)	R_q[b,f] (Å)	d_e[b] (e/Å^3)	footprint[b] (Å^2)	$\Gamma_{XRR,sqn}$[b] (nm^{-2})	Γ_{XRR}[b]/Γ_{CV}[a] ($\times 10^{-10}$ mol/cm^2)
F0	4.66	1.28	1.43	53	6.7	2.4	0.28	60	1.7	2.8/3.6
F2	4.80	1.30	2.61	44	8.0	2.7	0.37	44	2.3	3.8/2.3
F4	4.93	1.48	3.80	34	9.7	2.8	0.30	50	2.0	3.3/2.3
F6	5.27	1.65	3.79	48	7.9	2.7	0.38	54	1.9	3.1/1.8
F10	5.10	2.30	1.86	46	8.1	2.4	0.36	66	1.5	2.5/1.5
Bare ITO	5.41	2.32	NA	NA	NA	NA	NA	NA	NA	NA
PEDOT:PSS	5.3[c]	NA	NA	NA	400	NA	NA	NA	NA	NA

[a]On ITO. [b]On Si/SiO_2. [c]**PEDOT:PSS** work function from Huang et al.[2] [d]Dipole moment calculated via DFT modeling. [e]Tilt angle calculated and averaged from molecular lengths L1 to L4 in Figure 11. [f]Roughness is the derived fitting parameter for the IFL-air interface.

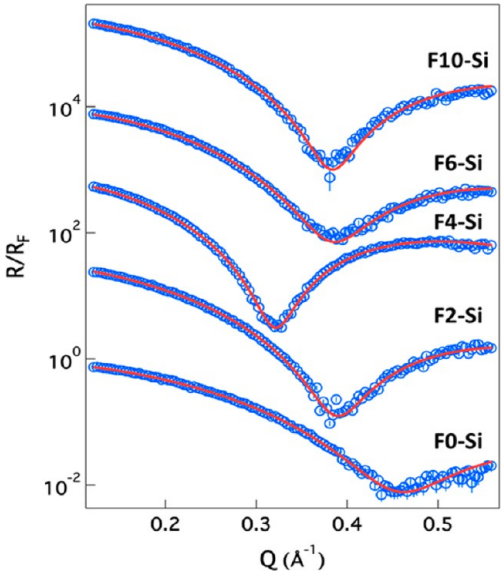

Figure 5. X-ray reflectivity data (blue circles), normalized to the Fresnel reflectivity; and the best-fit values (solid red lines) based on the single-slab models for the indicated IFLs **F0**- to **F10**−**Si**.

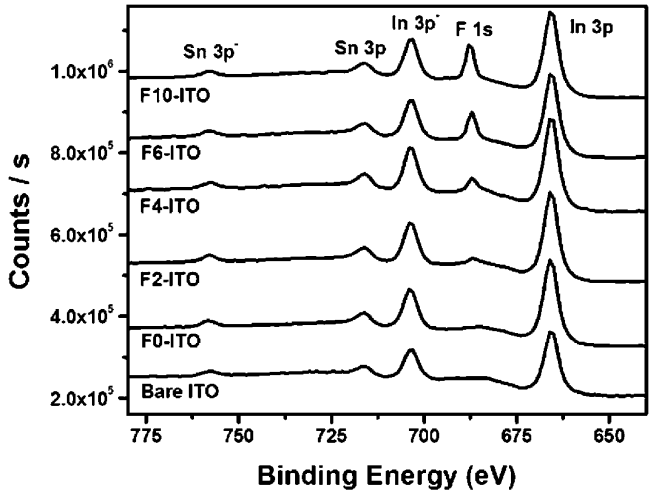

Figure 6. XPS spectra of bare and IFL/SAM-modified ITO surfaces depicting associated In, Sn, and F peaks. The F 1s peak intensity progressively increases through the series **F0-ITO** → **F10-ITO**, whereas In 3p peak and Sn 3p peak intensities remain approximately constant.

Trend wise, the XRR-derived packing density for each modified substrate is found generally to fall as the number of F substituents is increased, presumably reflecting increasing steric demands (Table 1). The exception is **F0**−**Si**. However, the deviation of the **F0**−**Si** film thickness and packing density from expectation likely originates in the lower precursor C−F functionalization level/electron density and attendant lower accuracy of the XRR data fitting.

X-ray Photoelectron Spectroscopy. The atomic compositions of the IFL-modified ITO surfaces were assayed by XPS and compared to that of **bare ITO**. The F: N atom % ratios are found to be 2.0, 3.92, 6.38, and 9.58 for the **F2-**, **F4-**, **F6-**, and **F10-ITO**, respectively. These results are in excellent agreement with theory and establish the existence of the fluoroaryl moieties on the glass/ITO surface. The progressive increase in the F 1s peak intensity is illustrated in Figure 6. The Cl:N at % ratios were used to estimate the remaining Cl-containing species on the surface, and were found to average ∼0.36, which is significantly less than expected for the precursors (i.e., 3) indicating near completion of silane conversion. XPS data are summarized in Table 2.

Grazing Incidence X-ray Diffraction. The crystallinity of the **Fn-Si** coatings was also assayed by grazing incidence X-ray diffraction (GIXD). For all GIXD incidence angles with the 30 s exposure time employed, only amorphous scattering is evident, with no indication of diffraction peaks (Figure 7). Amorphous scattering is not observed in the same region for the bare Si(100)/SiO_2 wafer,[81] arguing that the amorphous scattering arises from the SAM-IFL. Crystalline octadecylsilane (OTS) SAMs on Si/SiO_2 substrates are reported to have a Γ of ∼5 molecules per nm^2, and amorphous OTS SAMs on Si/SiO_2 have a Γ of ∼1/4 that of crystalline OTS.[82] Considering the bulkier **F$_n$PAPTSi** molecular shape and aforementioned XRR- (1.5−2.3 molecules/nm^2) and CV-derived (0.9−1.7 molecules/nm^2) surface coverage, the amorphous nature of the saturated **Fn-Si** SAM is not entirely unexpected.

Table 2. XPS at. % Data and Derived F: N and Cl:N Ratios[a]

index	ITO	F0-ITO	F2-ITO	F4-ITO	F6-ITO	F10-ITO
C 1s (%)	100.0	91.4	85.5	75.3	69.2	59.2
F 1s (%)	NA	NA	7.4	17.3	23.9	34.9
N 1s (%)	NA	3.9	3.7	4.4	3.7	3.6
Si 2p (%)	NA	2.6	2.1	1.5	2.0	1.4
Cl 2p (%)	NA	2.1	1.2	1.5	1.2	0.9
total %	100.0	100.0	99.9	100.0	100.0	100.0
F:N	NA	NA	2.00	3.92	6.38	9.58
Cl:N	NA	0.56	0.33	0.33	0.31	0.25

[a]In, Sn, and O atom percent omitted because peak signals are essentially invariant. These data are compiled in the Supporting Information (S8).

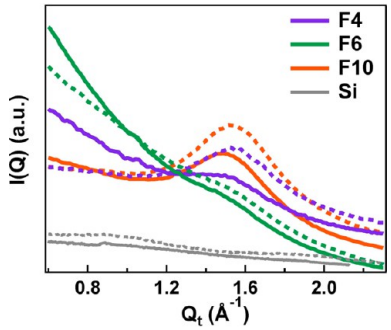

Figure 7. GIXD cross-cut spectra of IFL/SAM films on Si(100)/SiO_2. Solid and dashed lines represent in-plane and out-of-plane linecuts, respectively. Only the amorphous peak (1.5 A^{-1}) is detected from the modified substrates.

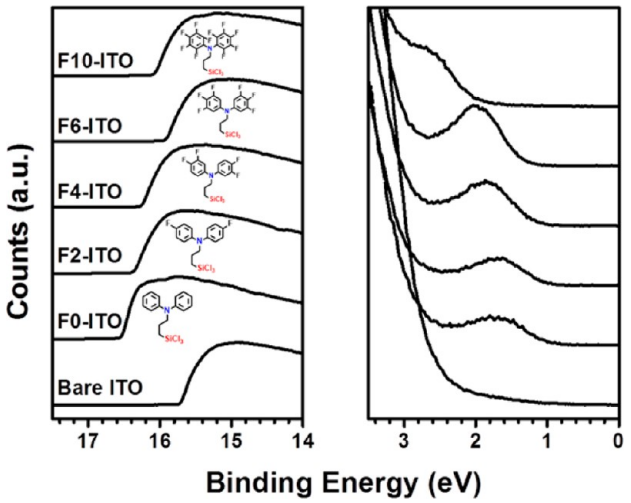

Figure 8. Normalized UPS analysis results for the **Fn-ITO** indicated. The work function shift is measured from the SECO, the cutoff energy of the highest binding energy. The HOMO energy is calculated from the summation of the work function and the VBM, the onset of the lowest binding energy.

UV Photoelectron Spectroscopy. UPS-derived work function (Φ_s) and ionization potential data for the **Fn-ITO** substrates are shown in Figure 8. Work functions are calculated from the difference between the secondary electron cutoff (SECO), the highest binding energy, and the He I source energy (21.22 eV),[83,84] and values range from 4.66 to 5.27 eV (Table 1). The valence band maximum (VBM) of the **Fn-ITO** relative to the Fermi level (0.0 eV) is determined from the onset of the lowest binding energy. The ionization potential, or HOMO, is then calculated using standard procedures from the sum of the derived work function and the VBM.[83,85]

The effectiveness of the SAM/IFL in selectively modifying the work function is evident from the UPS measurements, where the ITO work function is displaced to the range 4.66–5.27 eV, depending on the precursor structure (Table 1). The work function shift ($\Delta\Phi_s$), or the interfacial dipole, of **Fn-ITO** from clean ITO (4.7 eV)[31] is consistent with that predicted by the Helmholtz equation[86,87] (eq 2) with the dipole moment, μ, obtained from DFT computation, the SAM packing density, Γ,

$$\Delta\Phi_s = \frac{\mu\Gamma\cos\theta}{\varepsilon\varepsilon_0} \quad (2)$$

and tilt angle, θ, obtained from the XRR data, and with the physically reasonable assumption that the SAM absolute dielectric constant, $\varepsilon\varepsilon_0$, is proportional to N,[88,89] $\Delta\Phi_s$ correlates positively with the dipole moment of the SAM precursors. However, it will be seen that the OPV response characteristics as a function of $\Delta\Phi_s$ are not well correlated.

Cyclic Voltammetry. The redox potentials of the chemisorbed **F_nPAPTSi** molecules were measured in solution by CV (Figure 9) and compared to the HOMO energies determined by UPS and the computational modeling (see below). The CV-derived SAM precursor HOMOs were calculated from eq 3 as described by Liu et al.[90] and Al-Ibrahim et al.[91] where the vacuum level of Fc is set to 4.8 eV.

$$E_{HOMO} = -e[E_{onset} - Fc_{1/2}] - 4.8\ \text{eV} \quad (3)$$

The CV scan data for the **Fn-ITOs** and cross-linked **F_nPAPTSi** molecules adsorbed on Pt electrodes are shown in Figure 9f. In summary, the CV determined HOMO energies (blue bars) decrease as the aryl F substitution level increases, corresponding well with the UPS data (green bars) and computational modeling results (red bars) of Figure 10 (see below).

The surface physical and electronic properties of the **Fn-ITO** samples were analyzed by CV with varying scan rates. The full-width at half-maximum (fwhm) of the reversible **Fn-ITO** oxidation peaks (ν = 100 mV/s) from the first CV scan at 0.1 V/s were used to calculate the number of electrons transferred (n) where n = 90.6 mV/fwhm,[92] and these were determined to be one-electron processes for all SAMs. The SAM surface coverage (Γ_{CV}, Table 1) can be determined by integrating the oxidative peak, dividing by the scan rate to obtain the total charges transferred during oxidation, and then dividing the number of charges by the device area and the Faraday constant.[4,10] Overall, the Γ_{CV} values obtained electrochemically are in good agreement with the Γ_{XRR} data. Analysis to directly obtain heterogeneous electron transport rate constants for the **Fn-ITOs** by varying the scan rate was not possible due to peak diminution after several CV scans, suggesting decomposition at more extreme potentials.

Computational Modeling of IFL Structures. The geometrical optimization and Hessian calculation from the computational modeling was used to estimate SAM molecular properties. The optimized molecular geometries show the **F_nPAPTSi** structures to be similar across the series (Figure 11, see Experimental Section for more methodology details). The sum of the valence angles around the central N atom is invariably near 360°, indicating an essentially planar geometry around N, in agreement with experimental structural data for triarylamines.[50,51] **F_nPAPTSi** out-of-plane dipole moments (μ_z) were calculated from the SAM thicknesses measured by XRR and molecular lengths calculated from the optimized geometries. The van der Waals molecular dimensions were determined from the coordinates of the optimized geometries. For example, the computed coordinates of **F_4PAPTSi** and the van der Waals radius of the terminal Si atom, and the para-, and meta-position atoms on the aromatic rings were used for the molecular length, width, and depth calculation. Since the SAMs were determined to be amorphous from the GIXD measurements, it is assumed that the chemisorbed molecules can tilt over a range of angles. Thus, the molecular lengths determined as in Figure 11a, were used for tilt angle estimation. Once the average tilt angle was determined, the molecular dipole moment vector μ obtained from the Hessian calculation was used to project its out-of-plane component μ_z. The HOMO

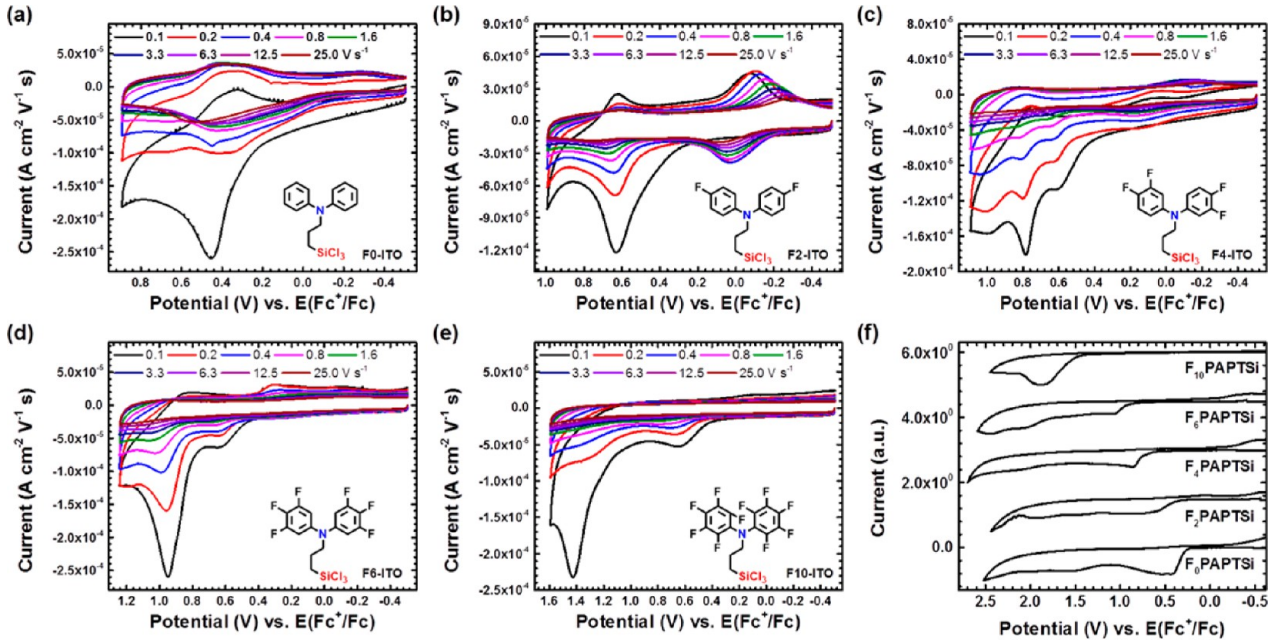

Figure 9. Cyclic voltammetry characterization of **Fn-ITOs**. All measurements carried out in an electrolyte of 0.1 M $(n\text{-Bu})_4N^+PF_6^-$ in anhydrous acetonitrile solution with an average electrode area of 0.75 cm^2. Fc was added after all measurements as internal standard. CVs of (a) **F0-**, (b) **F2-**, (c) **F4-**, (d) **F6-**, and (e) **F10-ITO** scanned at ν = 0.1, 0.2, 0.4, 0.8, 1.6, 3.2, 6.3, 12.5, and 25.0 V s^{-1}, respectively. (f) Cross-linked **F$_n$PAPTSi** series on a Pt working electrode scanned at ν = 0.1 V s^{-1}.

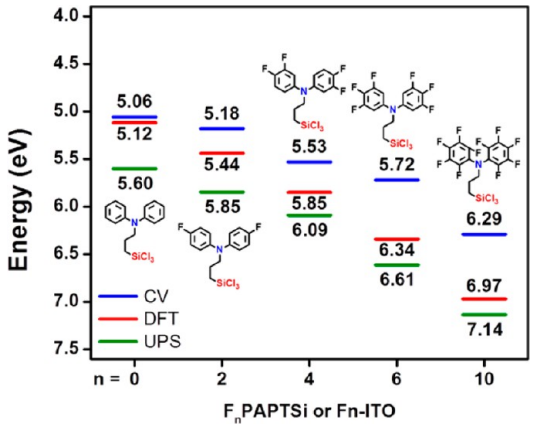

Figure 10. Comparison of HOMO energies of chemisorbed **F$_0$PAPTSi**, **F$_2$PAPTSi**, **F$_4$PAPTSi**, **F$_6$PAPTSi**, and **F$_{10}$PAPTSi** IFLs measured by cyclic voltammetry and computed by DFT/B3LYP. The ionization potentials of **F0-**, **F2-**, **F4-**, **F6-**, and **F10-ITO** by UV photoelectron spectroscopy are also plotted for comparison. The trend of HOMO energies calculated and measured by various techniques agrees well to each other.

energies of the **F$_n$PAPTSi** structures obtained from the Hessian calculation are found to follow the same trend as the HOMO energies determined from the experimental CV and UPS measurements. A tabulation of μ_z values and average molecular tilt angles is summarized in Table 1, and computed **F$_n$PAPTSi** HOMO energies using the optimized geometries are provided in Figure 10 above. Details of the μ_z calculations and lists of **F$_4$PAPTSi** atomic coordinates are provided in the Supporting Information (S7).

Indirect Determination of Heterogeneous Electron Transport Kinetics. Heterogeneous electron transport rate constants k_s were indirectly determined using Laviron's method,[93,94] and the experimental designs of Yang et al.,[95] and Yu et al.,[96] adopting Fc as the redox probe. Direct measurement of the **Fn-ITO** heterogeneous electron transport rate constants was not possible due to the irreversible nature of the **Fn-ITO** redox chemistry, as discussed above. The principal heterogeneous electron transport process can be associated with tunneling since the **Fn-ITO** oxidations ($E_{p,a}$ > 0.4 V vs E(Fc$^+$/Fc)) occur well beyond Fc oxidation ($E_{p,a}$ ≈ 0.2 V vs E(Fc$^+$/Fc)). Similar behavior was reported by Chidsey[97] and Smalley et al.[98] where SAMs on metal electrodes exhibit similar charge conduction

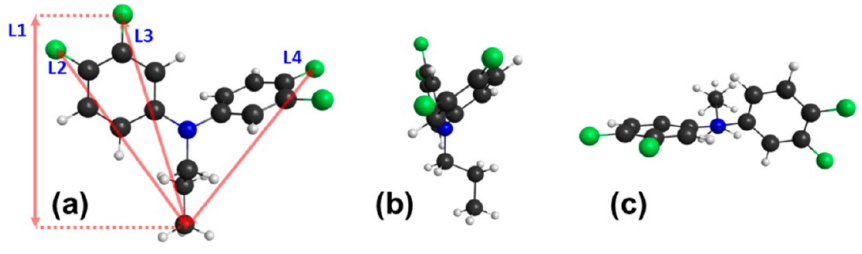

Figure 11. Representative DFT/B3LYP optimized geometry of a simplified model **F$_4$PAPTSi** IFL; (a) front view; (b) side view; (c) top view. The black, white, blue and green spheres represent C, H, N, and F atoms, respectively. The translucent red arrows in a show the various distances used for molecular tilt angle and μ_z determination.

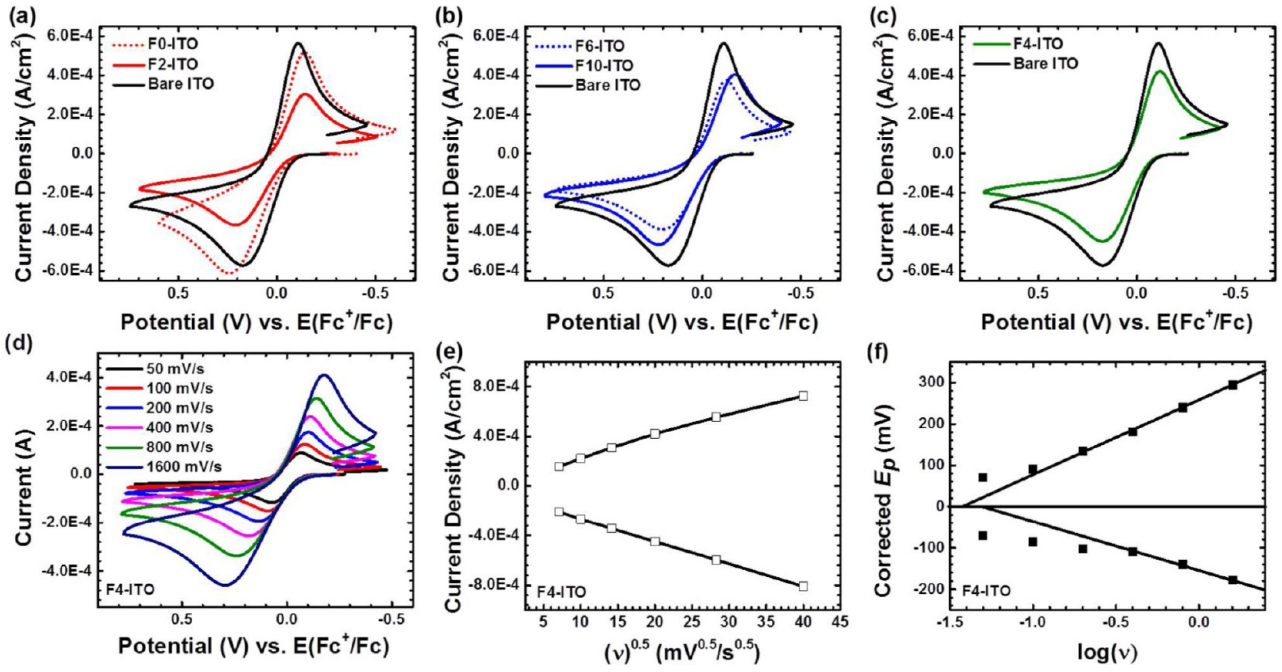

Figure 12. Cyclic voltammetry characterization of **Fn-ITOs**. All measurements carried out in 0.1 M $(n\text{-Bu})_4N^+PF_6^-$ electrolyte in anhydrous acetonitrile with 0.002 M Fc as redox probe. Average electrode area =0.58 cm^2. Measured Fc peaks in each scan corrected to Fc formal potential. (a) CVs of **F0-**, **F2-**, and **bare ITO**; scan rate = 400 mV/s. (b) CVs of **F6-**, **F10-**, and **bare ITO**; scan rate = 400 mV/s. (c) CVs of **F4-** and **bare ITOs** at scan rate = 400 mV/s. (d) CVs of **F4-ITO** at 50−1600 mV/s scan rates. (e) Current density vs (scan rate)$^{-1/2}$ for **F4-ITO**. Both oxidation and reduction branches are nearly linear. (f) Determination of linear region of corrected E_p vs log(ν) plot for **F4-ITO.** The asymmetric nature of linear region corresponds to $\alpha \neq 0.5$.

Table 3. IFL/Electrode Characteristics Determined by Cyclic Voltammetry

	slope		α		y-intercepts (mV)		
working electrode	Red	Ox	Red	Ox	Red	Ox	$k_s{}^a$ (s^{-1})
F0-ITO	−91.7	176	0.645	0.664	−183	319	0.203 ± 0.016
F2-ITO	−79.7	200	0.741	0.704	−179	295	0.350 ± 0.053
F4-ITO	−85.4	180	0.692	0.671	−154	256	0.495 ± 0.042
F6-ITO	−80.6	192	0.734	0.692	−149	282	0.469 ± 0.066
F10-ITO	−88.4	203	0.668	0.709	−198	318	0.209 ± 0.035
Bare ITO	−87.2	174	0.678	0.660	−135	247	0.601 ± 0.030

[a] k_s values calcuated from the average of α values from the reduction and oxidation branches.

properties. Representative scans of the Fc redox probe with **Fn-ITO** working electrodes are shown in Figure 12. From known properties of Fc, it is reasonable to assume one-electron redox events (n = 1) under these conditions.[99] The oxidation ($E_{p,a}$) and reduction ($E_{p,c}$) waves are recorded, corrected to the Fc formal potential, E^j = 624 mV,[100] and plotted against the scan rate (ν) on a log scale. The linear region ($\Delta E_p \geq 200$, where $\Delta E_p = E_{p,a} - E_{p,c}$) is determined, then the slope and y-intercept, ν_y.

A series of linear equations of oxidation/reduction branches is constructed according to eqs 4 and 5, where F, R, and T denote the Faraday constant, ideal gas constant, and temperature in Kelvin, respectively. α is the transfer coefficient, which gives the symmetry of the redox system energetic barrier.[92] The slopes, described by the first prelogarithmic terms in eqs 4 and 5 can be extracted from experimental E_p vs log ν plots and used to calculate α values from both the oxidative and reductive branches. In theory, α values extracted from each branch must be equal, but experimental uncertainty

$$E_{p,a} - E^j = \frac{2.303RT}{(1-\alpha)nF}\log \nu + \frac{2.303RT}{(1-\alpha)nF}\log\left(\frac{(1-\alpha)nF}{RTk_s}\right) \quad (4)$$

$$E_{p,c} - E^j = -\frac{2.303RT}{\alpha nF}\log \nu - \frac{2.303RT}{\alpha nF}\log\left(\frac{\alpha nF}{RTk_s}\right) \quad (5)$$

can affect the α values.[92,94] Thus, α values obtained from both branches were averaged and used in further calculations. Subtracting $E_{p,c}$ from $E_{p,a}$, eq 6 defines ΔE_p in terms of log ν. The second term in eq 6 is the intercept difference, $\Delta\nu_y$, (eq 7), i.e., the difference between the second terms of eqs 4 and 5. Equation 7 can then be rearranged to eq 8, to determine k_s. The present data reveal that **F4-ITO** has the largest k_s, followed by the progression: **F6-** > **F2-** > **F0-** ≈ **F10-ITO**. The slope, α, ν_y, and k_s for the **Fn-ITO** electrodes are summarized in Table 3. $E_{p,a}$ and $E_{p,c}$ data and plots of various electrode responses are in the Supporting Information (S9).

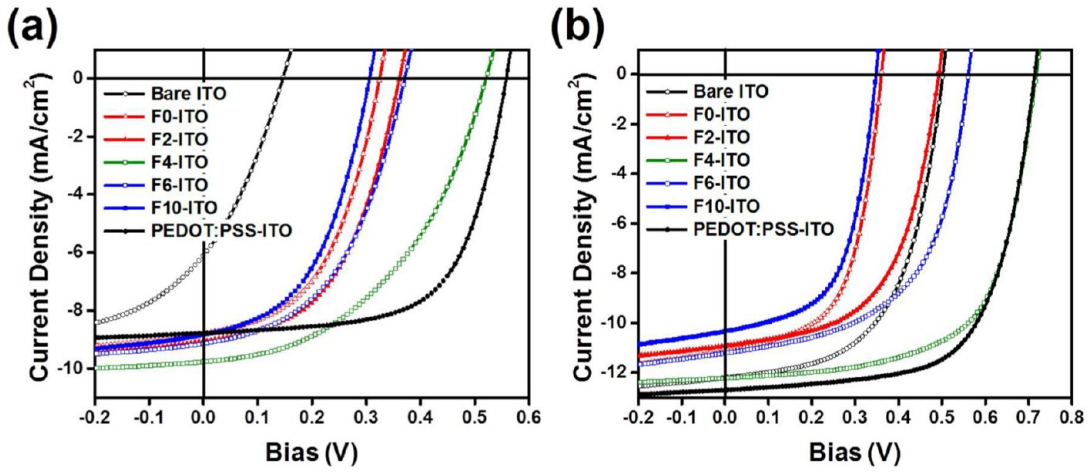

Figure 13. Average $J-V$ curves of (a) ITO/IFL/P3HT:PCBM/LiF/Al OPVs and (b) ITO/IFL/PTB7:PCBM/LiF/Al OPVs. **F0-**, **F2-**, **F4-**, **F6-**, **F10-**, **Bare**, and **PEDOT:PSS-ITO** denote the types of IFL used.

Table 4. Comparison of IFL Identity and Device Characteristics for P3HT:$PC_{71}BM$ and PTB7: $PC_{71}BM$-Based Solar Cells[a]

	V_{oc} (mV)		J_{sc} (mA/cm^2)		FF (%)		PCE (%)	
IFL	P3HT	PTB7	P3HT	PTB7	P3HT	PTB7	P3HT	PTB7
Bare ITO	170 ± 92	507 ± 30	7.4 ± 1.9	12.2 ± 0.7	38.1 ± 7.9	56.8 ± 3.2	0.66 ± 0.45	3.51 ± 0.16
F0-ITO	327 ± 37	359 ± 10	8.8 ± 0.2	10.9 ± 0.2	50.9 ± 3.0	58.4 ± 1.7	1.55 ± 0.27	2.28 ± 0.14
F2-ITO	373 ± 60	505 ± 45	9.1 ± 0.1	10.9 ± 0.2	52.1 ± 3.2	55.7 ± 2.6	1.91 ± 0.37	3.06 ± 0.22
F4-ITO	519 ± 58	717 ± 2	9.8 ± 0.2	12.2 ± 0.3	48.4 ± 8.5	64.1 ± 1.4	2.53 ± 0.69	5.62 ± 0.14
F6-ITO	392 ± 90	563 ± 25	9.1 ± 0.3	11.2 ± 0.4	51.9 ± 7.1	56.5 ± 2.9	1.99 ± 0.71	3.56 ± 0.16
F10-ITO	308 ± 32	346 ± 10	8.8 ± 0.2	10.3 ± 0.5	49.1 ± 2.9	58.1 ± 1.1	1.50 ± 0.24	2.08 ± 0.16
PEDOT:PSS	556 ± 20	708 ± 39	8.8 ± 1.2	12.7 ± 0.3	63.5 ± 3.1	68.8 ± 4.1	3.50 ± 0.64	6.19 ± 0.31

[a]Tabulated OPV parameters are the average of the best 5 pixels from 2 individual devices. The uncertainty range given is the first standard deviation of the averaged data.

$$\Delta E_p = \frac{2.303RT}{\alpha(1-\alpha)nF}\log \nu + \frac{2.303RT}{\alpha(1-\alpha)nF}\left[\alpha\log(1-\alpha) + (1-\alpha)\log\alpha - \log\left(\frac{RT}{nF}\right) - \log k_s\right] \quad (6)$$

$$\Delta\nu_y = \frac{2.303RT}{\alpha(1-\alpha)nF}\left[\alpha\log(1-\alpha) + (1-\alpha)\log\alpha - \log\left(\frac{RT}{nF}\right) - \log k_s\right] \quad (7)$$

$$\log k_s = \alpha\log(1-\alpha) + (1-\alpha)\log\alpha - \log\left(\frac{RT}{nF}\right) - \frac{\alpha(1-\alpha)nF\Delta\nu_y}{2.303RT} \quad (8)$$

A noteworthy feature here concerns the redox peak shift behavior with ν and current, I. SAM-modified electrodes typically exhibit significant positive $E_{p,a}$ shifts and reduced I versus bare electrodes due to poor charge conduction through the passivating organic layers.[101,102] For the present modified electrodes (Figure 12a–c), ΔE_p, the $E_{p,a}$ shifts of the **Fn-ITOs** versus **bare ITO** are small (<0.1 V) and the currents are reduced. This may reflect significant defect site densities permitting unperturbed Fc redox reactions,[101,103] or tunneling through the thin SAM (<1 nm) .[98,104−106] Sabatani et al.[101] showed that bulky head groups with short tethers to irregular ITO surfaces can yield dense but porous monolayers,[34,101] which may apply here. However, as noted above, Γ_{XRR} and Γ_{CV} (3.3 and 2.3 × 10^{-10} mol/cm^{-2} for **F4−Si** and **F4-ITO**, respectively, Table 1) are comparable to those reported for tightly packed $Fc(CO_2H)_2$/ITO monolayers (4.0 × 10^{-10} mol/cm^2),[34,107,108] and of the same order of magnitude as theoretical saturation densities estimated from the molecular dimensions. Furthermore, no obvious correlations are observed in the $k_s(\Gamma_{CV})$ plots (Supporting Information S11), and the shapes of the Fc redox curves among **Fn-ITO** electrodes are similar, implying that any effects of defect sites are either identical, which seems unrealistic, or more plausibly, too small to affect the charge transport process between the electrode and probe species.[102,103] Therefore, the bulk of the present Fc redox chemistry appears not to occur at defect sites, but rather via tunneling as reported by Chidsey,[97] Smalley,[98] and Devaraj.[104] There, tightly packed nonredox active alkyl SAM-coated electrodes transport charge as a function of temperature, electrode potential, and SAM thickness in a manner characteristic of tunneling.[109] Charge tunneling through SAMs with redox-active sites has also been reported by Cheng[105] and Wang.[110] Note that the present **Fn-ITO** ΔE_p values increase in the order: F4 < F6 < F2 < F10 < F0, closely paralleling the magnitudes of μ_z and k_s, with the k_s values more sensitive to the former than to Γ. The relationship between k_s and OPV performance is discussed below.

OPV Response. P3HT:$PC_{71}BM$ and PTB7:$PC_{71}BM$ bulk-heterojunction PV cells were fabricated with the glass/ITO/IFL

anodes described above. Averaged $J-V$ curves from the 5 best pixels of two different devices are shown in Figure 13. V_{oc}, J_{sc}, fill factor (FF), and PCE data for these devices are summarized in Table 4. Note that among the IFLs investigated, OPVs fabricated with **F4-ITO** exhibit the highest performance metrics, followed by the progression **F6-** > **F2-** > **F0-** > **F10-ITO**, and closely tracking the trends in k_s (see more below).

DISCUSSION

In this section, how SAM structure and packing density correlate with **Fn-ITO** structural and electronic properties are first discussed, followed by how these impact OPV performance, and finally how BHJ OPV active layer materials respond to carrier concentrations modulated by the **Fn-ITO** IFLs.

Surface Electronic Properties. Conventionally, k_s is used to describe the rates of solution-phase redox reactions[92,110,111] and electrocatalytic processes[112] at electrode surfaces, and is also correlated with the substrate conductance.[113] In case of quantum dot and dye-sensitized solar cells, the heterogeneous electron transport rate between the photoactive component and redox shuttle is used to characterize device performance.[114,115] In this study, k_s describes the redox kinetics between **Fn-ITO**s and a solution phase Fc redox probe. We inquire how analogous this is to the anode-active layer solid state OPV charge transport kinetics. Understanding the parameters governing k_s may provide insight into how IFLs modulate BHJ OPV performance.

The heterogeneous electron transport rate constants (k_s) of the IFL-modified ITO substrates are seen empirically to roughly correlate with the product of the IFL out-of-plane dipole moment (μ_z) times the CV-determined IFL surface coverage (Γ_{CV}; Figure 14). This suggests a relationship between the charge transfer rate, μ_z, and Γ as in eq 9, implying that

$$k_s \propto \mu_z \Gamma \tag{9}$$

larger IFL dipole moments create greater local electric fields, hence facilitate IFL charge transport, with the field strength scaling with the dipolar IFL packing density.[116] Interestingly, k_s and $\Delta\Phi_s$ (Figure 15a) are less well correlated, as are PCE and $\Delta\Phi_s$ (Figure 15b), where $\Delta\Phi_s$ is defined as the difference between the **Fn-ITO** work function (Φ_s) and the clean ITO work function (4.7 eV).[31,45] The term $\mu_z\Gamma$ in eq 9 resembles the term $\mu\Gamma\cos\theta$ in eq 2. Thus, the rather weak $k_s - \Delta\Phi_s$ correlation implies that those factors underlying k_s are more complex than the work function alone. The other factors in eq 9 likely include orbital energies, IFL thickness, and tunneling constant which will be discussed elsewhere as discussed below.

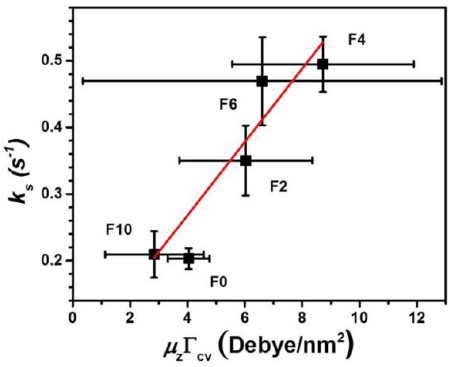

Figure 14. Plot of k_s vs the product of $\mu_z \times \Gamma_{CV}$. The Pearson's correlation of a linear fit (red solid line) is 0.92.

Note that the superior performance of the OPVs fabricated with **F4-ITO** correlates with the largest k_s of the present IFL series. Note also that OPVs fabricated with several of the glass/ITO/IFL anodes exhibit higher performance than OPVs fabricated with a bare glass/ITO anode having a greater k_s (0.601 s^{-1}, Table 3). This result is consistent with the **Fn-ITO** anodes having greater charge selectivity (electron-blocking) characteristics than the bare glass/ITO anode due to a relatively high LUMO, or suppression of thermoionic emission by the IFL acting as a tunneling barrier,[33,117] and a dipolar orientation which favors hole rather than electron collection.[33]

OPV Performance as a Function of IFL. To understand the effects of inserting a thin anode dipolar layer on BHJ OPV PCE, V_{oc}, J_{sc}, and FF, we plotted data as a function of k_s in Figure 16. Note that PCE is a function of the three OPV performance parameters (eq 10) where P_0 (100 mW/cm^2) is

$$\mathrm{PCE} = \frac{V_{oc} J_{sc} \mathrm{FF}}{P_0} \tag{10}$$

the light power under AM 1.5G.[31] Nevertheless, PCE can be used to examine the viability of k_s as an OPV characterization metric. As noted above, **F4-ITO** has the largest heterogeneous electron transport rate constant followed by **F6-**, **F2-**, **F0-**, and **F10-ITO**. Interestingly, the present OPV parameters exhibit nearly identical trends with k_s, except for FF, which exhibits no obvious trend. The corresponding parameters for **PEDOT:PSS** and **bare ITO** are not included since very different surface chemistry likely occurs in the CV measurements. Furthermore, the correlation between anode work function and device parameters is observed to be marginal for all the present ITO/IFL-based OPVs (Figure 17). Initially, V_{oc}, J_{sc}, and PCE of PTB7- and P3HT-based OPVs rise as the work function increases; however, this trend weakens beyond work functions greater than 4.9 eV. Work function also does not explain the origin of FF fluctuations in these OPVs, and further investigation will be required to understand the abrupt PCE fall with work function the **F10-** and **F6-ITO**-based OPVs.

The present correlations of V_{oc} and J_{sc} with k_s conform to a model suggested by Kirchartz[118] and Wagenpfahl,[119] where the electrode carrier extraction rate governs overall OPV current until the electrode carrier extraction capacity exceeds the charge production in the active layer. The electrode carrier extraction rate is defined as the rate of majority carrier (hole here) extraction from the bulk active layer at the electrode (anode here). If the hole extraction rate is slow, the carrier density at the interface increases, therefore the charge recombination rate in the active layer increases, leading to a fall in V_{oc}, J_{sc}, and PCE.[120] Conversely, OPV metrics would be enhanced by effectively eliminating the charge accumulation at the interface if the hole extraction rate is high. The enhancement then continues until the hole extraction rate surpasses hole output from the active layer, then the enhancement saturates. As seen in Figure 16, a strong positive correlation between k_s and OPV metrics indeed exists. Furthermore, while the P3HT- and PTB7-based OPVs perform similarly at low k_s values, the PTB7-based OPV metrics are enhanced greatly from those of the **F4-ITO** IFL (the anode with the highest k_s), whereas P3HT-based OPV metrics are enhanced moderately with the same anode. All other factors being equal, PTB7-based OPVs produce significantly higher J_{sc}s than do P3HT-based OPVs,

dx.doi.org/10.1021/am4030609 | ACS Appl. Mater. Interfaces 2013, 5, 9224−9240

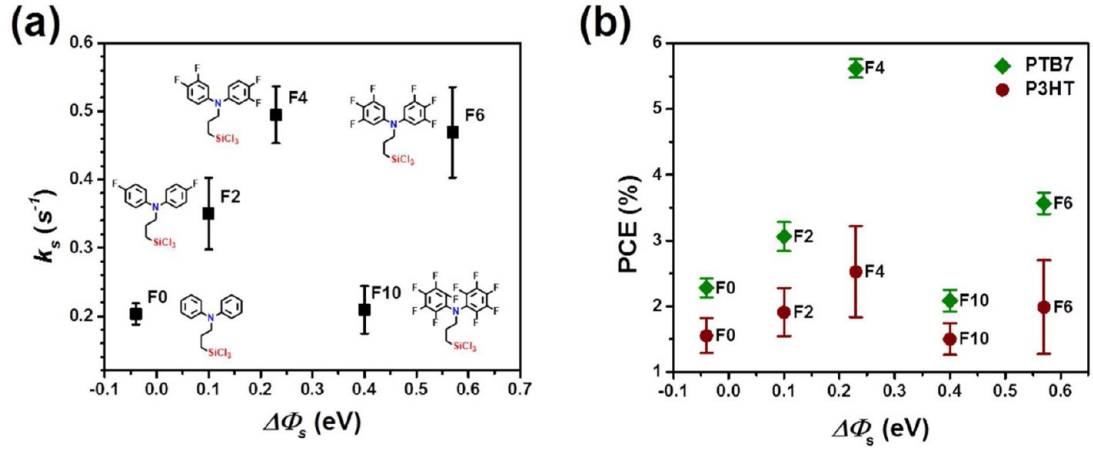

Figure 15. (a) Plot of k_s vs the ITO/SAM interfacial dipole, and (b) a plot of PCE vs the interfacial dipole. Interfacial dipole is calculated by subtracting ITO work function (4.7 eV) from the **Fn-ITO** work functions (Φ_s).

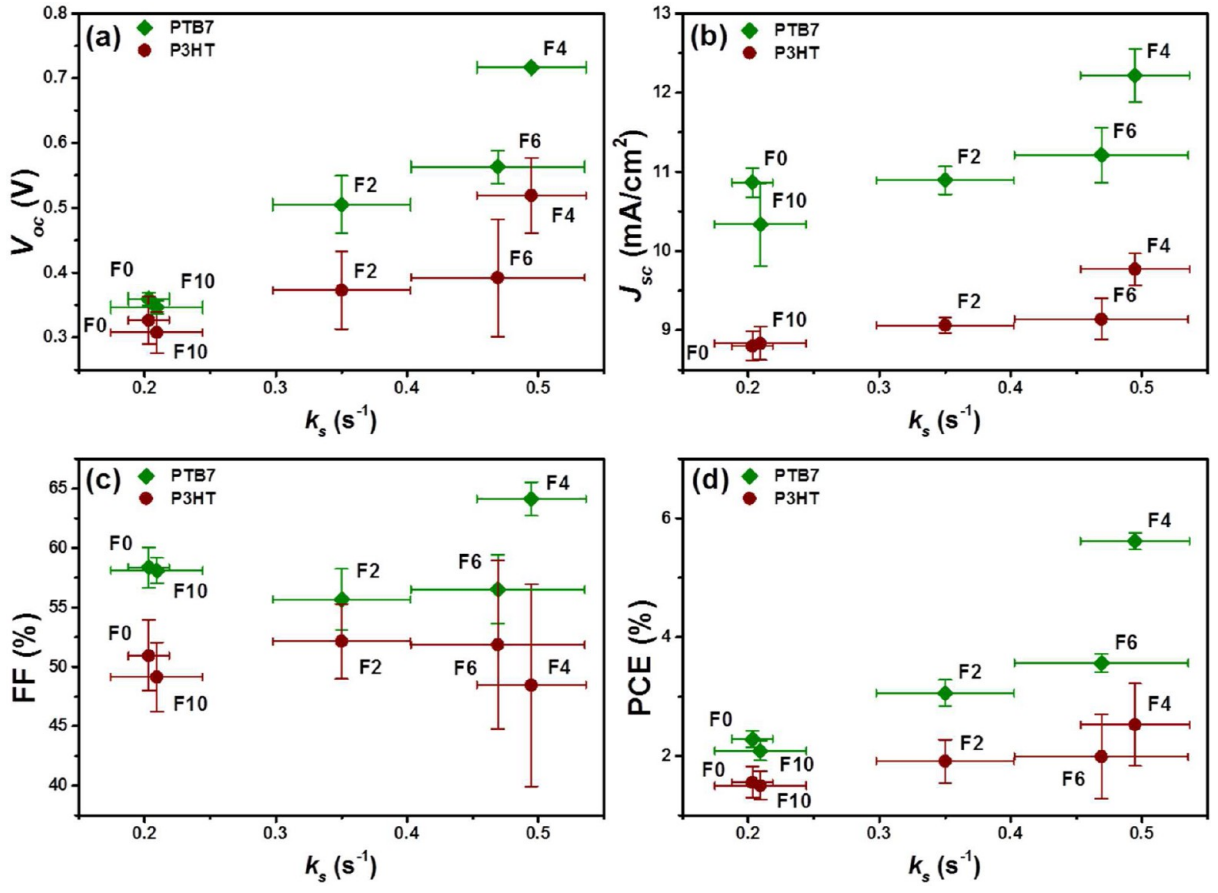

Figure 16. OPV device metrics vs k_s: (a) V_{oc} vs k_s, (b) J_{sc} vs k_s, (C) FF vs k_s, and (d) PCE vs k_s. Device performance characteristics of PTB7- (green diamonds) and P3HT- based (brown circles) OPVs with one standard deviation and k_s with error range are represented. Except FF, V_{oc}, J_{sc}, and PCE are positively correlated with the anode k_s.

because J_{sc} scales with the (carrier density) × (mobility).[106,115,116] Thus, PTB7-based OPVs require more rapid charge carrier extraction than do the P3HT-based OPVs. Note also that the PTB7 and P3HT OPV metrics have not saturated at k_s = 0.5 s^{-1} and a further enhancement is expected with higher k_s electrodes. In conclusion, a low k_s electrode can be a significant bottleneck for OPVs, and higher performing OPV active layer materials such as PTB7 might be further improved with even higher k_s anodes.

In summary, the **F4-ITO** anode is ideally suited for rapid interfacial charge transport due to the high k_s, μ_z, and Γ metrics. This results in the highest hole extraction rate among the series of IFL-modified anodes and leads to the highest OPV V_{oc}, J_{sc}, and thus PCE values. That is, the **F4-ITO** anode has the highest capacity to extract photogenerated holes from the OPV active layer. Therefore, one expects densely packed and highly dipolar SAMs with high k_s values will become essential to accommodate next-generation active layer materials with even

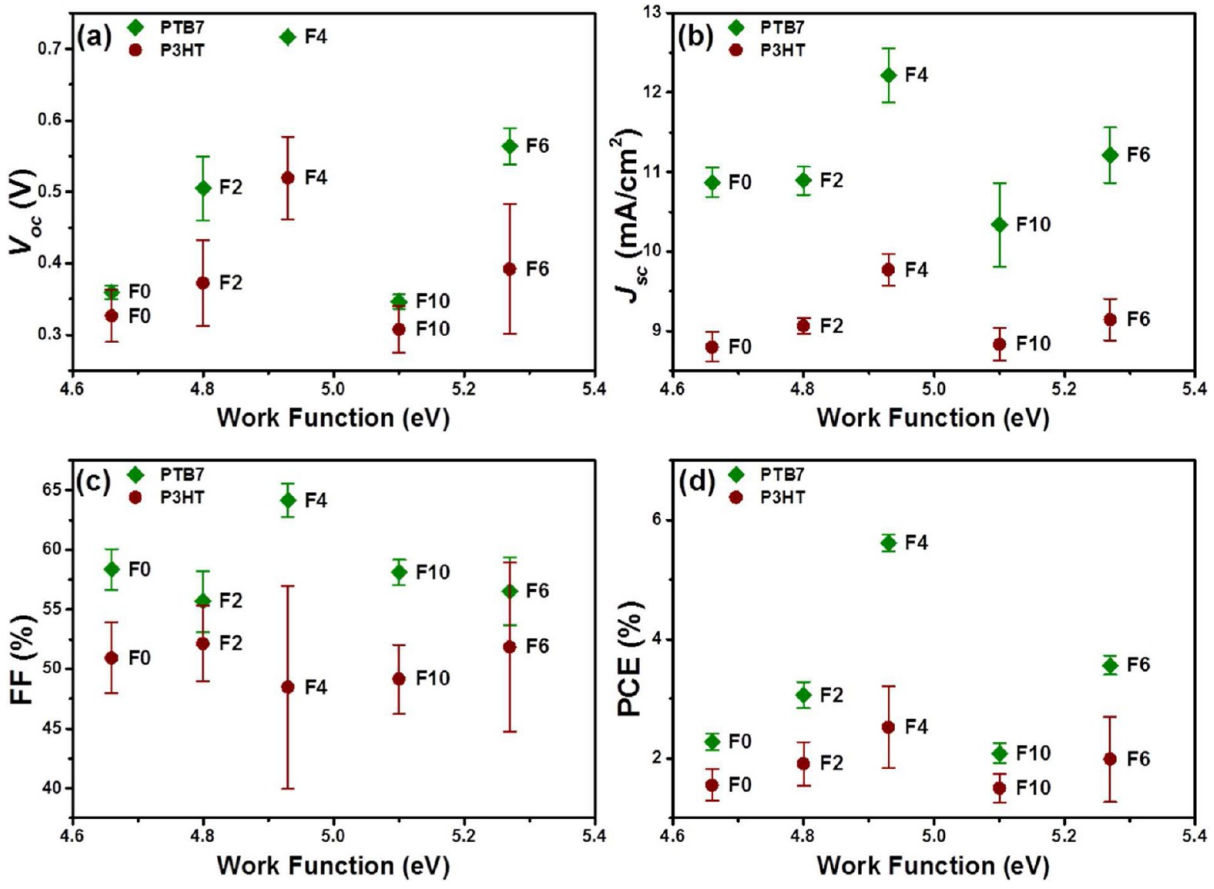

Figure 17. Plots of work function vs OPV performance metrics for PTB7- (green diamonds) and P3HT-based (brown circles) devices at one standard deviation: (a) V_{oc} vs work function, (b) J_{sc} vs work function, (C) FF vs work function, and (d) PCE vs work function. Up to work function ~4.9 eV, PCE rises as work function increases, but the trend deviates afterward.

higher charge carrier densities and mobilities under illumination.

CONCLUSIONS

A novel series of silane-tethered bis(fluoroaryl)amine IFL precursors for functionalizing glass/ITO surfaces has been synthesized and characterized. As assessed by advancing contact angles, AFM, XPS, DFT calculations, UPS, and cyclic voltammetry, the resulting SAMs are smooth, well-packed, hydrophobic monolayers with tunable HOMO energies, work functions, and heterogeneous electron transfer rate constants. OPVs fabricated with these SAM-modified anodes exhibit V_{oc}, J_{sc} and therefore PCE metrics that most closely track the cyclic voltammetry-derived heterogeneous electron transport rate constants, k_s values. It is moreover experimentally found for the first time that k_s scales as the SAM out-of-plane dipole moment and surface coverage, to enhance hole extraction and suppress recombination processes.

ASSOCIATED CONTENT

Supporting Information

SAM characterization: AFM image and data, contact angle measurement data with side view images, XPS survey spectra, and XRR parameter fitting method for SAM optimization. Molecular geometry: The coordinate of DFT assisted optimized geometry of **F_4PAPTSi** and the method for calculating a molecular dimension. CV data of **Fn-ITO**s and NMR data for molecular characterization are also included. This material is available free of charge via the Internet at http://pubs.acs.org.

AUTHOR INFORMATION

Corresponding Authors

*E-mail: t-marks@northwestern.edu.
*E-mail: bedzyk@northwestern.edu.
*E-mail: l-chen@northwestern.edu.

Notes

The authors declare no competing financial interest.

ACKNOWLEDGMENTS

Research supported in part Argonne-Northwestern Solar Energy Research (ANSER) Center, an Energy Frontier Research Center funded by the U.S. Department of Energy, Office of Science, Office of Basic Energy Sciences, under Award DE-SC0001059 (S.J.L.; A.T.) and by the U.S. Department of Energy, Office of Science, and Office of Basic Energy Sciences under Award DE-AC02-06CH11357 (L.X.C) and DE-FG02-08ER46536 (C.K.S.). We thank Integrated Molecular Structure Education and Research Center (IMSERC) for characterization facilities supported by Northwestern University (NU) and National Science Foundation (NSF) under NSF CHE-0923236 and CHE-9871268 (1998), Pfizer, State of Illinois, and IMSERC mass spectrometer staffs for analyzing the mass of newly synthesized precursor molecules. Research was also supported in part by the NSF funded MRSEC under DMR-1121262 (Z.L.; J.D.E.; M.J.B.). The XRR measurements were

made at the MRSEC X-ray Diffraction Facility located at NU. Use of the Advanced Photon Source at Argonne National Laboratory was supported by the U.S. Department of Energy, Office of Science, Office of Basic Energy Sciences, under Contract DE-AC02-06CH11357. We also thank Prof. R. J. Thomson for synthetic advice, J. L. Song for mathematical derivations, and Dr. J. Smith, Dr. S. M. Yoon, and Dr. M.-G. Kim for helpful discussions.

REFERENCES

(1) Hains, A. W.; Ramanan, C.; Irwin, M. D.; Liu, J.; Wasielewski, M. R.; Marks, T. J. *ACS Appl. Mater. Interfaces* **2010**, *2*, 175−185.
(2) Hains, A. W.; Marks, T. J. *Appl. Phys. Lett.* **2008**, *92*, 023504.
(3) Lee, T.-W.; Chung, Y. *Adv. Funct. Mater.* **2008**, *18*, 2246−2252.
(4) Huang, Q.; Evmenenko, G. A.; Dutta, P.; Lee, P.; Armstrong, N. R.; Marks, T. J. *J. Am. Chem. Soc.* **2005**, *127*, 10227−10242.
(5) Brabec, C. J.; Shaheen, S. E.; Winder, C.; Sariciftci, N. S.; Denk, P. *Appl. Phys. Lett.* **2002**, *80*, 1288−1290.
(6) Huang, Q.; Evmenenko, G.; Dutta, P.; Marks, T. J. *J. Am. Chem. Soc.* **2003**, *125*, 14704−14705.
(7) Yan, H.; Lee, P.; Armstrong, N. R.; Graham, A.; Evmenenko, G. A.; Dutta, P.; Marks, T. J. *J. Am. Chem. Soc.* **2005**, *127*, 3172−3183.
(8) Cui, J.; Huang, Q.; Veinot, J. G. C.; Yan, H.; Marks, T. J. *Adv. Mater.* **2002**, *14*, 565−569.
(9) Veinot, J. G. C.; Marks, T. J. *Acc. Chem. Res.* **2005**, *38*, 632−643.
(10) Huang, Q.; Li, J.; Evmenenko, G. A.; Dutta, P.; Marks, T. J. *Chem. Mater.* **2006**, *18*, 2431−2442.
(11) Liang, Y.; Xu, Z.; Xia, J.; Tsai, S.-T.; Wu, Y.; Li, G.; Ray, C.; Yu, L. *Adv. Mater.* **2010**, *22*, 1−4.
(12) Jorgensen, M.; Norrman, K.; Krebs, F. C. *Sol. Energy Mater. Sol. Cells* **2008**, *92*, 686−714.
(13) de Jong, M. P.; van Ijzendoorn, L. J.; de Voigt, M. J. A. *Appl. Phys. Lett.* **2000**, *77*, 2255−2257.
(14) Kim, H.; Nam, S.; Lee, H.; Woo, S.; Ha, C.-S.; Ree, M.; Kim, Y. *J. Phys. Chem. C* **2011**, *115*, 13502−13510.
(15) Manceau, M.; Rivaton, A.; Gardette, J.-L.; Guillerez, S.; Lemaitre, N. *Sol. Energy Mater. Sol. Cells* **2011**, *95*, 1315−1325.
(16) Burrows, P. E.; Bulovic, V.; Forrest, S. R.; Sapochak, L. S.; Mccarty, D. M.; Thompson, M. E. *Appl. Phys. Lett.* **1994**, *65*, 2922−2924.
(17) Reese, M. O.; Morfa, A. J.; White, M. S.; Kopidakis, N.; Shaheen, S. E.; Rumbles, G.; Ginley, D. S. *Sol. Energy Mater. Sol. Cells* **2008**, *92*, 746−752.
(18) Armstrong, N. R.; Carter, C.; Donley, C.; Simmonds, A.; Lee, P.; Brumbach, M.; Kippelen, B.; Domercq, B.; Yoo, S. *Thin Solid Films* **2003**, *445*, 342−352.
(19) Kemerink, M.; Timpanaro, S.; De Kok, M. M.; Meulenkamp, E. A.; Touwslager, F. J. *J. Phys. Chem. B* **2004**, *108*, 18820−18825.
(20) Pingree, L. S. C.; MacLeod, B. A.; Ginger, D. S. *J. Phys. Chem. C* **2008**, *112*, 7922−7927.
(21) Timpanaro, S.; Kemerink, M.; Touwslager, F. J.; De Kok, M. M.; Schrader, S. *Chem. Phys. Lett.* **2004**, *394*, 339−343.
(22) Nardes, A. M.; Kemerink, M.; Janssen, R. A. J.; Bastiaansen, J. A. M.; Kiggen, N. M. M.; Langeveld, B. M. W.; van Breemen, A. J. J. M.; De Kok, M. M. *Adv. Mater.* **2007**, *19*, 1196−1200.
(23) Brumbach, M.; Veneman, P. A.; Marrikar, F. S.; Schulmeyer, T.; Simmonds, A.; Xia, W.; Lee, P.; Armstrong, N. R. *Langmuir* **2007**, *23*, 11089−11099.
(24) Khodabakhsh, S.; Sanderson, B. M.; Nelson, J.; Jones, T. S. *Adv. Funct. Mater.* **2006**, *16*, 95−100.
(25) Hau, S. K.; Cheng, Y.-J.; Yip, H.-L.; Zhang, Y.; Ma, H.; Jen, A. K.-Y. *ACS Appl. Mater. Interfaces* **2010**, *2*, 1892−1902.
(26) Yip, H.-L.; Hau, S. K.; Baek, N. S.; Ma, H.; Jen, A. K.-Y. *Adv. Mater.* **2008**, *20*, 2376−2382.
(27) Hau, S. K.; Yip, H.-L.; Ma, H.; Jen, A. K.-Y. *Appl. Phys. Lett.* **2008**, *93*, 104−113.
(28) Sharma, A.; Haldi, A.; Potscavage, W. J.; Hotchkiss, P. J.; Marder, S. R.; Kippelen, B. *J. Mater. Chem.* **2009**, *19*, 5298−5302.
(29) Murray, I. P.; Lou, S. J.; Cote, L. J.; Loser, S.; Kadleck, C. J.; Xu, T.; Szarko, J. M.; Rolczynski, B. S.; Johns, J. E.; Huang, J.; Yu, L.; Chen, L. X.; Marks, T. J.; Hersam, M. C. *J. Phys. Chem. Lett.* **2011**, *2*, 3006−3012.
(30) Li, S.-S.; Tu, K.-H.; Lin, C.-C.; Chen, C.-W.; Chhowalla, M. *ACS Nano* **2010**, *4*, 3169−3174.
(31) Irwin, M. D.; Buchholz, B.; Hains, A. W.; Chang, R. P. H.; Marks, T. J. *Proc. Natl. Acad. Sci. U.S.A.* **2008**, *105*, 2783−2787.
(32) Yuan, Y.; Reece, T. J.; Sharma, P.; Poddar, S.; Ducharme, S.; Gruverman, A.; Yang, Y.; Huang, J. *Nat. Mater.* **2011**, *10*, 296−302.
(33) Ratcliff, E. L.; Garcia, A.; Paniagua, S. A.; Cowan, S. R.; Giordano, A. J.; Ginley, D. S.; Marder, S. R.; Berry, J. J.; Olson, D. C. *Adv. Energy Mater.* **2013**, *3*, 647−656.
(34) Hotchkiss, P. J.; Jones, S. C.; Paniagua, S. A.; Sharma, A.; Kippelen, B.; Armstrong, N. R.; Marder, S. R. *Acc. Chem. Res.* **2012**, *45*, 337−346.
(35) Beaumont, N.; Hancox, I.; Sullivan, P.; Hatton, R. A.; Jones, T. S. *Energy Environ. Sci.* **2011**, *4*, 1708−1711.
(36) Song, C. K.; White, A. C.; Zeng, L.; Leever, B. J.; Clark, M. D.; Emery, J. D.; Lou, S. J.; Chen, L. X.; Bedzyk, M. J.; Marks, T. J. *Prepr.−Am. Chem. Soc., Div. Energy Fuels* **2013**, *58*, 351−352.
(37) Aswal, D. K.; Lenfant, S.; Guerin, D.; Yakhmi, J. V.; Vuillaume, D. *Anal. Chim. Acta* **2006**, *568*, 84−108.
(38) Ulman, A., *An Introduction to Ultrathin Organic Films: From Langmuir−Blodgett to Self-Assembly*, 1st ed.; Academic Press: New York, 1991.
(39) Helmy, R.; Fadeev, A. Y. *Langmuir* **2002**, *18*, 8924−8928.
(40) Gershewitz, O.; Grinstein, M.; Sukenik, C. N.; Regev, K.; Ghabboun, J.; Cahen, D. *J. Phys. Chem. B* **2004**, *108*, 664−672.
(41) Iimura, K.-I.; Kato, T.; Morita, S.-I.; Ozaki, Y. *Mol. Cryst. Liq. Cryst. Sci. Technol., Sect. A* **1999**, *337*, 113−116.
(42) Materne, T.; de Buyl, F.Witucki, G. L. *Organosilane Technology in Coating Applications: Review and Perspectives*; Dow Corning: Midland, MI, 2012; p 16.
(43) Kim, J. S.; Park, J. H.; Lee, J. H.; Jo, J.; Kim, D.-Y.; Cho, K. *Appl. Phys. Lett.* **2007**, *91*, 112111.
(44) Peor, N.; Sfez, R.; Yitzchaik, S. *J. Am. Chem. Soc.* **2008**, *130*, 4158−4165.
(45) Hotchkiss, P. J.; Li, H.; Paramonov, P. B.; Paniagua, S. A.; Jones, S. C.; Armstrong, N. R.; Bredas, J.-L.; Marder, S. R. *Adv. Mater.* **2009**, *21*, 4496−4501.
(46) Chung, Y.; Verploegen, E.; Vailionis, A.; Sun, Y.; Nishi, Y.; Murmann, B.; Bao, Z. *Nano Lett.* **2011**, *11*, 1161−1165.
(47) Hau, S. K.; Yip, H.-L.; Acton, O.; Baek, N. S.; Ma, H.; Jen, A. K.-Y. *J. Mater. Chem.* **2008**, *18*, 5113−5119.
(48) Yip, H. L.; Hau, S. K.; Baek, N. S.; Jen, A. K.-Y. *Appl. Phys. Lett.* **2008**, *92*, 193313.
(49) Veregin, R. P.; Harbour, J. R. *J. Phys. Chem.* **1990**, *94*, 6231−6237.
(50) Sobolev, A. N.; Belsky, V. K.; Romm, I. P.; Chernikova, N. Y.; Guryanova, E. N. *Acta Crystallogr., Sect. C* **1985**, *41*, 967−971.
(51) Malagoli, M.; Bredas, J. L. *Chem. Phys. Lett.* **2000**, *327*, 13−17.
(52) Ratcliff, E. L.; Zacher, B.; Armstrong, N. R. *J. Phys. Chem. Lett.* **2011**, *2*, 1337−1350.
(53) Lou, S. J.; Szarko, J. M.; Xu, T.; Yu, L. P.; Marks, T. J.; Chen, L. X. *J. Am. Chem. Soc.* **2011**, *133*, 20661−20663.
(54) Wipf, P.; Maciejewski, J. P. *Org. Lett.* **2008**, *10*, 4383−4386.
(55) Moran, R. J.; Cramer, C.; Falvey, D. E. *J. Org. Chem.* **1997**, *62*, 2742−2751.
(56) Koppang, R. *Acta Chem. Scand.* **1971**, *25*, 3067−3071.
(57) Hohenberg, P.; Kohn, W. *Phys. Rev.* **1964**, *136*, B864.
(58) Kohn, W.; Sham, L. J. *Phys. Rev.* **1965**, *140*, 1133.
(59) *Modern Density Functional Theory: A Tool for Chemistry*; Seminario, J. M., Polizter, P., Eds.; Elsevier Science: Amsterdam, 1995.
(60) Koch, W.; Holthausen, M. C., *A Chemist's Guide to Density Functional Theory*, 2nd ed.; Wiley-VCH: Weinheim, Germany, 2001.
(61) Johnson, B. G.; Gill, P. M. W.; Pople, J. A. *J. Chem. Phys.* **1993**, *98*, 5612−5626.
(62) Parr, R. G. *Annu. Rev. Phys. Chem.* **1983**, *34*, 631−656.

(63) Vosko, S. H.; Wilk, L.; Nusair, M. *Can. J. Phys.* **1980**, *58*, 1200−1211.
(64) Lee, C.; Yang, W.; Parr, R. G. *Phys. Rev. B: Condens. Matter Mater. Phys.* **1988**, *37*, 785−789.
(65) Becke, A. D. *J. Chem. Phys.* **1993**, *98*, 5648−5652.
(66) Stephens, P. J.; Devlin, F. J.; Chabalowski, C. F.; Frisch, M. J. *J. Phys. Chem.* **1994**, *98*, 11623−11627.
(67) Francl, M. M.; Pietro, W. J.; Hehre, W. J.; Binkley, J. S.; Gordon, M. S.; Defrees, D. J.; Pople, J. A. *J. Chem. Phys.* **1982**, *77*, 3654−3665.
(68) Schmidt, M. W.; Baldridge, K. K.; Boatz, J. A.; Elbert, S. T.; Gordon, M. S.; Jensen, J. H.; Koseki, S.; Matsunaga, N.; Nguyen, K. A.; Su, S. J.; Windus, T. L.; Dupuis, M.; Montgomery, J. A. *J. Comput. Chem.* **1993**, *14*, 1347−1363.
(69) Shao, Y.; Molnar, L. F.; Jung, Y.; Kussmann, J.; Ochsenfeld, C.; Brown, S. T.; Gilbert, A. T. B.; Slipchenko, L. V.; Levchenko, S. V.; O'Neill, D. P.; DiStasio, R. A., Jr.; Lochan, R. C.; Wang, T.; Beran, G. J. O.; Besley, N. A.; Herbert, J. M.; Yeh Lin, C.; Van Voorhis, T.; Hung Chien, S.; Sodt, A.; Steele, R. P.; Rassolov, V. A.; Maslen, P. E.; Korambath, P. P.; Adamson, R. D.; Austin, B.; Baker, J.; Byrd, E. F. C.; Dachsel, H.; Doerksen, R. J.; Dreuw, A.; Dunietz, B. D.; Dutoi, A. D.; Furlani, T. R.; Gwaltney, S. R.; Heyden, A.; Hirata, S.; Hsu, C.-P.; Kedziora, G.; Khalliulin, R. Z.; Klunzinger, P.; Lee, A. M.; Lee, M. S.; Liang, W.; Lotan, I.; Nair, N.; Peters, B.; Proynov, E. I.; Pieniazek, P. A.; Min Rhee, Y.; Ritchie, J.; Rosta, E.; David Sherrill, C.; Simmonett, A. C.; Subotnik, J. E.; Lee Woodcock Iii, H.; Zhang, W.; Bell, A. T.; Chakraborty, A. K.; Chipman, D. M.; Keil, F. J.; Warshel, A.; Hehre, W. J.; Schaefer Iii, H. F.; Kong, J.; Krylov, A. I.; Gill, P. M. W.; Head-Gordon, M. *Phys. Chem. Chem. Phys.* **2006**, *8*, 3172−3191.
(70) Bode, B. M.; Gordon, M. S. *J. Mol. Graphics Modell.* **1998**, *16*, 133−138.
(71) Owens, D. K.; Wendt, R. C. *J. Appl. Polym. Sci.* **1969**, *13*, 1741.
(72) You, Z. Z. *Mater. Lett.* **2007**, *61*, 3809−3814.
(73) Fukuto, M.; Heilmann, R. K.; Pershan, P. S.; Yu, S. M.; Soto, C. M.; Tirrell, D. A. *J. Chem. Phys.* **2003**, *119*, 6253−6270.
(74) Gagne, R. R.; Koval, C. A.; Lisensky, G. C. *Inorg. Chem.* **1980**, *19*, 2854−2855.
(75) Perales, J. B.; Van Vranken, D. L. *J. Org. Chem.* **2001**, *66*, 7270−7274.
(76) Paniagua, S. A.; Hotchkiss, P. J.; Jones, S. C.; Marder, S. R.; Mudalige, A.; Marrikar, F. S.; Pemberton, J. E.; Armstrong, N. R. *J. Phys. Chem. C* **2008**, *112*, 7809−7817.
(77) Terrill, R. H.; Tanzer, T. A.; Bohn, P. W. *Langmuir* **1998**, *14*, 845−854.
(78) Vacca, P.; Petrosino, M.; Miscioscia, R.; Nenna, G.; Minarini, C.; Della Sala, D.; Rubino, A. *Thin Solid Films* **2008**, *516*, 4232−4237.
(79) Badre, C.; Pauporte, T.; Turmine, M.; Lincot, D. *Superlattices Microstruct.* **2007**, *42*, 99−102.
(80) Chuang, I.-S.; Maciel, G. E. *J. Phys. Chem. B* **1997**, *101*, 3052−3064.
(81) Warren, B. E. *J. Am. Ceram. Soc.* **1934**, *17*, 249−254.
(82) Ito, Y.; Virkar, A. A.; Mannsfeld, S.; Oh, J. H.; Toney, M.; Locklin, J.; Bao, Z. *J. Am. Chem. Soc.* **2009**, *131*, 9396−9404.
(83) Yi, Y.; Lyon, J. E.; Beerbom, M. M.; Schlaf, R. *J. Appl. Phys.* **2006**, *100*, 093719.
(84) Cho, S.; Seo, J. H.; Lee, K.; Heeger, A. J. *Adv. Funct. Mater.* **2009**, *19*, 1459−1464.
(85) Schroeder, P. G.; France, C. B.; Park, J. B.; Parkinson, B. A. *J. Phys. Chem. B* **2003**, *107*, 2253−2261.
(86) Oliveira, O. N.; Taylor, D. M.; Lewis, T. J.; Salvagno, S.; Stirling, C. J. M. *J. Chem. Soc., Faraday Trans.* **1989**, *85*, 1009−1018.
(87) Bruening, M.; Cohen, R.; Guillemoles, J. F.; Moav, T.; Libman, J.; Shanzer, A.; Cahen, D. *J. Am. Chem. Soc.* **1997**, *119*, 5720−5728.
(88) Romaner, L.; Heimel, G.; Ambrosch-Draxl, C.; Zojer, E. *Adv. Funct. Mater.* **2011**, *21*, 3406.
(89) Romaner, L.; Heimel, G.; Ambrosch-Draxl, C.; Zojer, E. *Adv. Funct. Mater.* **2008**, *18*, 3999−4006.
(90) Liu, Y.; Liu, M. S.; Jen, A. K.-Y. *Acta Polym.* **1999**, *50*, 105−108.
(91) Al-Ibrahim, M.; Roth, H.-K.; Zhokhavets, U.; Gobsch, G.; Sensfuss, S. *Sol. Energy Mater. Sol. Cells* **2005**, *85*, 13−20.
(92) Eckermann, A. L.; Feld, D. J.; Shaw, J. A.; Meade, T. J. *Coord. Chem. Rev.* **2010**, *254*, 1769−1802.
(93) Laviron, E.; Roullier, L. *J. Electroanal. Chem.* **1980**, *115*, 65−74.
(94) Laviron, E. *J. Electroanal. Chem.* **1979**, *101*, 19−28.
(95) Yang, J.; Strickler, J. R.; Gunasekaran, S. *Nanoscale* **2012**, *4*, 4594−4602.
(96) Yu, H.-Z.; Boukherroub, R.; Morin, S.; Wayner, D. D. M. *Electrochem. Commun.* **2000**, *2*, 562−566.
(97) Chidsey, C. E. D. *Science* **1991**, *251*, 919−922.
(98) Smalley, J. F.; Sachs, S. B.; Chidsey, C. E. D.; Dudek, S. P.; Sikes, H. D.; Creager, S. E.; Yu, C. J.; Feldberg, S. W.; Newton, M. D. *J. Am. Chem. Soc.* **2004**, *126*, 14620−14630.
(99) Tsierkezos, N. G. *J. Solution Chem.* **2007**, *36*, 289−302.
(100) Pavlishchuk, V. V.; Addison, A. W. *Inorg. Chim. Acta* **2000**, *298*, 97−102.
(101) Sabatani, E.; Cohen-Boulakia, J.; Bruening, M.; Rubinstein, I. *Langmuir* **1993**, *9*, 2974−2981.
(102) Sabatani, E.; Rubinstein, I. *J. Phys. Chem.* **1987**, *91*, 6663−6669.
(103) Chailapakul, O.; Crooks, R. M. *Langmuir* **1995**, *11*, 1329−1340.
(104) Devaraj, N. K.; Decreau, R. A.; Ebina, W.; Collman, J. P.; Chidsey, C. E. D. *J. Phys. Chem. B* **2006**, *110*, 15955−15962.
(105) Cheng, J.; Robinson, D. B.; Cicero, R. L.; Eberspacher, T.; Barrelet, C. J.; Chidsey, C. E. D. *J. Phys. Chem. B* **2001**, *105*, 10900−10904.
(106) Creager, S.; Yu, C. J.; Bamdad, C.; O'Connor, S.; MacLean, T.; Lam, E.; Chong, Y.; Olsen, G. T.; Luo, J. Y.; Gozin, M.; Kayyem, J. F. *J. Am. Chem. Soc.* **1999**, *121*, 1059−1064.
(107) Donley, C.; Dunphy, D.; Paine, D.; Carter, C.; Nebesny, K.; Lee, P.; Alloway, D.; Armstrong, N. R. *Langmuir* **2002**, *18*, 450−457.
(108) Zotti, G.; Schiavon, G.; Zecchin, S.; Berlin, A.; Pagani, G. *Langmuir* **1998**, *14*, 1728−1733.
(109) Wolf, U.; Arkhipov, V. I.; Bassler, H. *Phys. Rev. B: Condens. Matter Mater. Phys.* **1999**, *59*, 7507−7513.
(110) Wang, W.; Li, X.; Wang, X.; Shang, H.; Liu, X.; Lu, X. *J. Phys. Chem. B* **2010**, *114*, 10436−10441.
(111) Ritzert, N. L.; Rodríguez-López, J.; Tan, C.; Abruña, H. D. *Langmuir* **2013**, *29*, 1683−1694.
(112) Yin, H.; Ma, Q.; Zhou, Y.; Ai, S.; Zhu, L. *Electrochim. Acta* **2010**, *55*, 7102−7108.
(113) Zhou, X.-S.; Liu, L.; Fortgang, P.; Lefevre, A.-S.; Serra-Muns, A.; Raouafi, N.; Amatore, C.; Mao, B.-W.; Maisonhaute, E.; Schöllhorn, B. *J. Am. Chem. Soc.* **2011**, *133*, 7509−7516.
(114) Kamat, P. V. *Acc. Chem. Res.* **2012**, *45*, 1906−1915.
(115) Tefashe, U. M.; Nonomura, K.; Vlachopoulos, N.; Hagfeldt, A.; Wittstock, G. *J. Phys. Chem. C* **2012**, *116*, 4316−4323.
(116) Monti, O. L. A. *J. Phys. Chem. Lett.* **2012**, *3*, 2342−2351.
(117) Yang, H.-T.; Shen, Y.-D.; Edwall, D.; Miller, D. L.; Harris, J. S. *IEEE Trans. Electron Devices* **1980**, *27*, 851−856.
(118) Kirchartz, T.; Pieters, B. E.; Taretto, K.; Rau, U. *J. Appl. Phys.* **2008**, *104*, 094513.
(119) Wagenpfahl, A.; Deibel, C.; Dyakonov, V. *IEEE J. Sel. Top. Quantum Electron.* **2010**, *16*, 1759−1763.
(120) Phillips, J. E.; Birkmire, R. W.; McCandless, B. E.; Meyers, P. V.; Shafarman, W. N. *Phys. Status Solidi B* **1996**, *194*, 31−39.